LABEL-FREE BIOSENSOR BASED UPON A VERTICALLY EMITTING DISTRIBUTED FEEDBACK LASER

BY

CHUN GE

THESIS

Submitted in partial fulfillment of the requirements
for the degree of Master of Science in Electrical and Computer Engineering
in the Graduate College of the
University of Illinois at Urbana-Champaign, 2010

Urbana, Illinois

Adviser:

Professor Brian T. Cunningham

ABSTRACT

Firstly, a novel fabrication strategy combining a nano-replica molding technique and a horizontal dipping technique has been demonstrated for the fabrication of solid state organic distributed feedback laser (DFB) biosensors. The combined techniques enable the organic DFB laser to be uniformly fabricated over large surface areas upon a flexible plastic substrate, with an approach that is compatible with roll-based manufacturing.

Secondly, laser pump threshold from a distributed feedback (DFB) structure, based upon a second order grating in a dye-doped polymer, has been efficiently reduced by implementing a resonant optical pumping scheme. The proposed scheme couples the excitation laser light into a resonant mode and takes advantage of the intensified electromagnetic field. For a Bragg grating having a periodicity of 400 nm, a Rhodamine 590 doped polymer laser operates at 584 nm and concurrently supports a resonance mode at 532 nm which is the excitation laser wavelength. Pumped under the resonant condition, the DFB laser exhibits a pump threshold reduction of 25-fold. In addition, the resonant optical pumping technique also enhances the light conversion efficiency by a factor of 23. This technique improves the performance of organic DFB lasers.

Finally, we demonstrate that a dielectric nanorod structure could be used to enhance the label-free detection sensitivity of the vertically emitting distributed feedback laser biosensor (DFBLB). We show that the use of the nanostructured film results in a three-dimensional volume overlap between the DFBLB resonant mode and the region in

which the biomolecule adsorption can occur. This modification in device design results in a ~6.6× increase in detection sensitivity while maintaining a narrowband output.

ACKNOWLEDGMENTS

My study at the University of Illinois at Urbana-Champaign is one of the most memorable periods of my life. I felt very fortunate to have learned from and worked with so many incredible people. First of all, I would like to thank my adviser, Professor Brian T. Cunningham, who has given me the opportunity to work on an exciting and interdisciplinary project and set a perfect example for both my academic and personal lives. His boundless energy, continual encouragement, and devotion to his students have been truly inspirational.

I am also deeply indebted to current and past members of the nano sensor group, including Meng Lu, Wei Zhang, Nikhil Ganesh, Ian Block, Leo Chan, Kashif Altaf, Patrick Mathias, Charles Choi, Fuchyi Yang, Sherine George, Ryan Hsin-Yu Wu, Erich Lidstone, Vikram Chaudhery, Alysia Belobraydich, and Anja Kohl.

This project was made possible by a cooperative agreement that was awarded and administered by the U.S. Army Medical Research & Materiel Command (USAMRMC) and the Telemedicine & Advanced Technology Research Center (TATRC), under Contract #: W81XWH0810701. I also extend my gratitude to the support staff of the Micro and Nanotechnology Laboratory at the University of Illinois at Urbana-Champaign.

I want to deeply thank my friends and my whole family. Especially, I want to thank my parents for always believing in me and blessing me.

TABLE OF CONTENTS

CHAPTER 1

INTRODUCTION

In the past 20 years, numerous optical devices have been investigated for sensitive label-free biomolecule sensing. Label-free optical biosensors based upon detection of transmitted or reflected spectra from passive optical resonators have found wide applications in life science research, environmental monitoring, quality control testing, pharmaceutical drug discovery and diagnostic testing [1-3]. Resonant optical structures such as photonic crystal surfaces [3], silicon oxide ring resonators [4], thin-walled glass capillaries [5], and microtoroids [6] generally detect resonant wavelength shift due to the interaction between captured target molecules and the evanescent electric field of the resonant modes, where the amount of wavelength shift is proportional to the density of immobilized biomaterial on the sensor surface. Such sensors are designed to have extremely smooth surfaces to minimize optical losses due to scattering in order to maintain a high Q-factor for wavelength resolution. Recently, optical biosensors based upon solid state organic DFB lasers fabricated upon plastic surfaces have been demonstrated as active optical resonators that obtain high Q-factor through the process of stimulated emission. Operating with single mode, narrow linewidth emission [7], DFB laser biosensors (DFBLB) are simultaneously capable of high sensitivity and a high degree of resolution.

Solid state organic lasers have attracted considerable attention since their first demonstration in 1967 by Soffer [8]. Because plastic-based lasers may be fabricated upon inexpensive substrates using fabrication approaches such as ink-jet printing to create patterned multilayer structures, they hold promise for applications that include optical communications, video display, and biosensors [7, 9]. Given their wide potential applications, many efforts has been devoted to improving their performance and fabrication process over the years. Researchers have already demonstrated a room temperature replica molding process for producing submicron grating features used for photonic crystal biosensors [10] and photonic crystal enhanced-fluorescence substrates for biochemical assays [11]. The process for these devices involves roll-to-roll manufacturing of the grating structure, as well as roll-to-roll deposition of SiO_2 and TiO_2 sputtered dielectric thin films. Recently, a novel process called "horizontal dipping" has been demonstrated as an effective method for producing thin polymer films used in organic light-emitting diodes (OLED) [12]. It turns out that this technique can be easily and conveniently incorporated into the fabrication of DFB laser biosensors. We demonstrated that the combination of the nano-replica molding technique and the horizontal dipping technique enables the organic DFB laser to be uniformly fabricated over large surface areas upon a flexible plastic substrate, with an approach that is compatible with roll-based manufacturing, which is an efficient manufacturing paradigm widely applied in industry.

Since the demonstrations (in 1971) of lasing in which optical feedback was provided by a corrugated, periodic refractive index structure, organic dyes have offered a

versatile gain medium for the evaluation of integrated resonator designs, waveguide configurations and microlaser fabrication techniques. DFB structures are generally preferred for solid state dye lasers, principally because end-on or out-of-plane emission, broad tunability, and narrow linewidth, are available with DFB-based oscillators. The DFB dye lasers were usually made by either periodic gain modulation or periodic refractive index modulation. A drawback of current organic DFB dye laser designs, however, is their high threshold, which usually necessitates a nano-second pulse laser as pumping light source. Therefore, an efficient pumping paradigm which could improve the stimulation emission threshold and the quantum efficiency of DFB lasers is highly desirable. In this thesis, we will present a resonant pumping strategy which couples the pumping light into a supported resonant mode of the DFB cavity and takes advantage of the resulting intensified electromagnetic field to improve both lasing pump threshold and energy conversion efficiency.

Finally, the DFB laser biosensor's surface sensitivity is investigated. Previously, DFBLB sensors have been demonstrated that incorporate a thin solid film of TiO_2 as the uppermost surface, where a 40-80 nm thick layer of TiO_2 serves to bias the resonant mode to reside more fully within the liquid media in contact with the DFBLB surface, thus providing a strong dependency of the emission wavelength on the density of adsorbed biomolecules [13]. Here, we demonstrate that a nanostructured high refractive index layer of TiO_2 nanorods may be used in place of a thin solid film of TiO_2. The use of the nanostructured film results in a three-dimensional volume overlap between the DFBLB resonant mode and the region in which biomolecule adsorption can occur. This

modification in device design results in a ~6.6× increase in the sensor's detection sensitivity.

The rest of this chapter is organized as follows. Section 1.1 describes the motivation behind designing a DFB laser biosensor. Section 1.2 shows the structure of the vertically emitting organic DFB laser biosensor. Section 1.3 describes the measurement setup that is used in most of the experiments reported in this work.

1.1 Motivation

The DFB laser biosensor is categorized as a resonant optical biosensor. Such sensors generally detect the resonant wavelength shift due to the interaction between captured target molecules and the evanescent electric field of the resonant modes, where the amount of wavelength shift is proportional to the density of immobilized biomaterial on the sensor surface. Here, the resonant mode is the lasing mode and the resonant wavelength is the laser emission wavelength.

Over the past decades, researchers have demonstrated different types of resonant optical biosensors, such as surface plasmon resonance biosensor (SPR) [14], photonic crystal surface biosensor [3, 5], microring [4], microsphere [7, 8], and microtoroid biosensor [9]. These biosensors vary in terms of sensitivity and resolution. All are classified as passive cavity resonant optical biosensors, which means they do not generate their own light, but only select a specific frequency or wavelength out of the input light signal. For such biosensors, the sensor's resolution can be evaluated from the

linewidth of the resonant peak, or equivalently, the quality factor, or Q-factor, of the resonant cavity, defined as

$$Q = \frac{\Delta \nu}{\nu_0} \tag{1}$$

where $\Delta \nu$ is the full-width at half-maximum (FWHM) of the resonant peak in terms of frequency, and ν_0 is the resonant frequency. The narrower the resonant peak or the higher the Q-factor, the better the resolution. A fair way to evaluate a biosensor's sensitivity is to measure the resonant wavelength shift due to the binding of a well-known protein, such as streptavidin, which is a 52,800 Dalton tetrameric protein widely used in molecule biology. When both the surface sensitivity and the resolution are taken into account, their product, which is referred to as the figure of merit (FOM), can be used as a yardstick to evaluate the performance of different kinds of label-free biosensors. Based on such a standard, Table 1.1 summarizes and compares the sensitivity and resolution of the passive cavity biosensors mentioned above.

Table 1.1 Sensitivity and resolution comparison.

Resonant biosensor	Q-factor	Streptavidin shift (nm)	Q-factor × Shift (FOM)
SPR	~15	14	0.2×10^3
Photonic crystal surface	1000	10	10^4
Microring	10^4-10^6	0.15	1.5×10^3-1.5×10^5
Microsphere	10^7	0.02	2×10^5
Microtoroid	10^8	0.0003	3×10^4
DFB laser	2×10^4	3.5	7×10^4

The goal of biosensing is to develop low cost biosensors with both high sensitivity and good resolution. However, there seems to be a trade-off between these characteristics for these passive resonant biosensors. Better sensitivity requires stronger interaction between the evanescent electric field and the target molecules that are immobilized on the sensor's surface. This strong coupling demands the resonant electric field to be extracted from the resonant cavity and results in a degraded Q-factor of the resonant cavity. For example, as summarized in Table 1.1, microrings, microsphere and microtoroid based biosensors have demonstrated impressive Q-factors due to the ability to strongly confine light within a high refractive index dielectric cavity. While these

approaches can demonstrate excellent resolution, as the Q-factor increases, it becomes increasingly more difficult to couple light out of the resonator, resulting in decreased sensitivity and dynamic detection range. Additionally, such biosensors also demand nanometer-level precision for positioning of optical fibers or waveguides to the resonator perimeter and also call for high-precision tunable lasers as the illumination source. All of these requirements just increase the complexity of the measurements, compromise the detection throughput and increase the detection cost. One way to address this issue is to build laser-based active cavity biosensors. Unlike its passive counterparts, a laser biosensor generates its own narrow linewidth output through the process of stimulated emission. Therefore, the DFB laser biosensor achieves high resolution and maintains good sensitivity at the same time. As Table 1.1 indicates, the DFB laser based biosensor stands out from its passive counterparts when both the resolution and sensitivity are taken into account.

1.2 Vertically Emitting Organic DFB Laser Structure

The optical cavity used for the DFB laser is a corrugated waveguide in which optical feedback is provided by the continuous coherent backscattering from the periodic material refractive index modulation. The cross section of the DFB laser is sketched in Figure 1.1. If this corrugated structure possesses gain, the optical cavity will emit light through stimulated emission when it absorbs pumped energy. The resonant wavelength of the cavity satisfies the Bragg condition,

$$\lambda = 2n_{eff}\Lambda/m \tag{1.2}$$

where m is the Bragg grating order, Λ denotes the grating period, and n_{eff} represents the effective refractive index. It can be seen from the Bragg condition that the order of Bragg grating affects not only the resonant wavelength but also the laser radiation pattern. For vertically emitting DFB laser, a second-order Bragg grating is utilized to result in radiation output nearly normal to the resonator surface by first-order grating diffraction. Such a vertically emitting property of the DFB laser facilitates the design of the output signal detection system. A fast and simple output signal analyzer is critical to achieve a practical biosensor system. Therefore, the vertically emitting DFB laser is adopted to build a label-free biosensor.

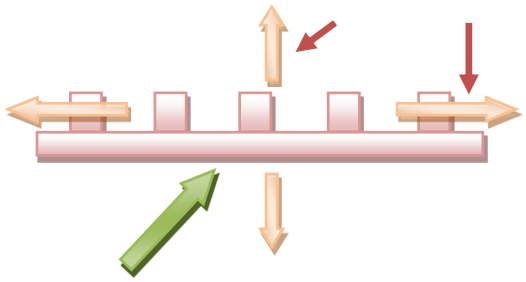

Fig. 1.1 Cross sections of second-order Bragg grating resonator. The DFB laser incorporates a second-order Bragg grating that supports both vertical emission and edge emission.

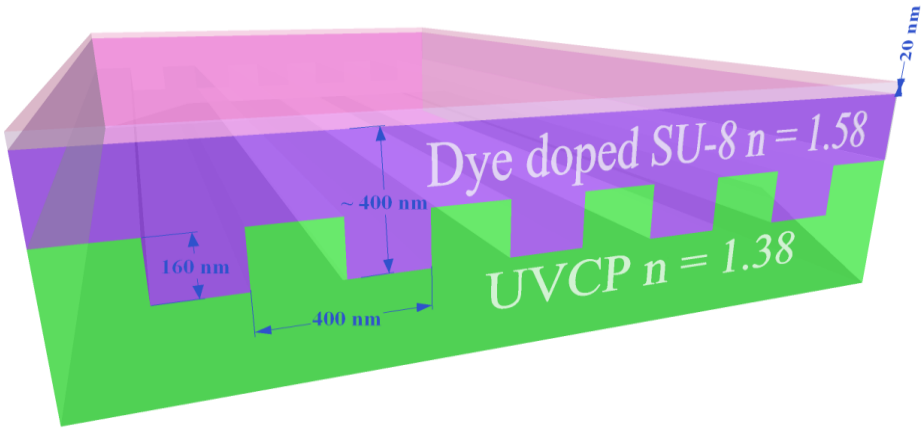

Fig. 1.2 Schematic of the DFB laser sensor.

A cross-sectional diagram (not to scale) of the vertically emitting DFB laser structure is shown in Fig. 1.2. The second-order Bragg grating is formed on the surface of a low refractive index polymer substrate. Upon the grating substrate is the dye doped SU-8 layer which serves as the active layer providing vertical light confinement, horizontal light feedback and light amplification. The laser dye doped polymer has the advantage of wide wavelength tuning range. It has been shown that the DFB laser using laser dye doped polymer can operate in a wavelength regime from green to near IR. Thereafter, a high-refractive-index thin dielectric film (TiO_2) is deposited on the top surface to improve the DFB laser sensor sensitivity and make the sensor surface biocompatible.

The material refractive index change, induced by bulk material change or molecular interactions, introduces shifts in the resonant wavelength of the DFB laser cavity. In other words, the DFB laser emission wavelength depends on the material coated on the sensor surface. The tracking of the laser emission wavelength reveals the kinetic evolution of the material mass density accumulated on the laser sensor surface.

The designed DFB laser sensor is optically pumped and the resulting stimulated emission is monitored along an axis nearly orthogonal to the surface by a fiber-coupled spectrometer.

1.3 Experiment Setup

Figure 1.3 is a schematic diagram of the experimental setup used to characterize the performance of the fabricated DFB laser. Optical pumping is provided by a frequency-doubled, Q-switched Nd: YAG pulse laser (λ_p = 532 nm, yttrium aluminum garnet) with pulse duration of 10 ps at a maximum repetition rate of 10 Hz. The pumping beam passes through a spatial filter and a 10× beam expander and a spatial filter to spatially clean the beam. Focused by a 10× objective, the pumping beam forms a ~20 μm diameter spot on the DFB laser surface which is placed right on the focal plane of the objective.

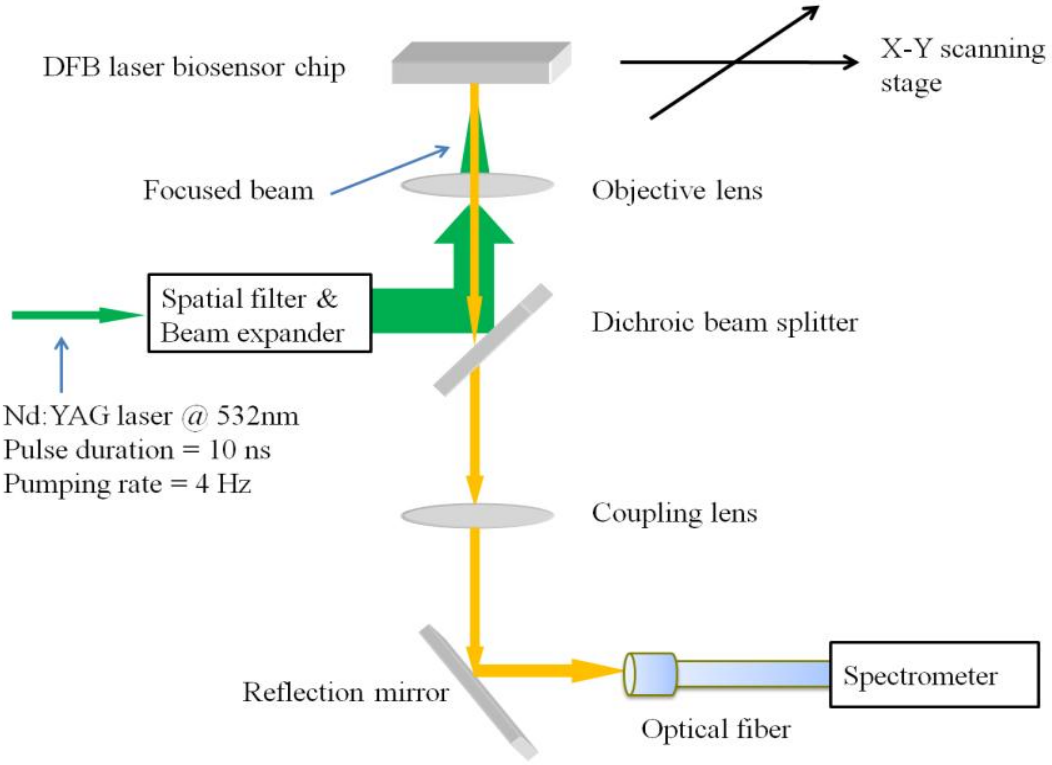

Fig. 1.3 Schematic of the biosensor detection instrument setup

The lasing emission from the device is collected by the same objective and then passes through a dichroic mirror and a long pass emission filter which eliminates the strong pumping light. Because the one-dimensional (1D) DFB resonator only provides confinement perpendicular to grating axis, the beam highly diverges along the direction that parallel to the grating axis. To account for this effect, the stimulated emission is coupled into a step index multimode fiber (d = 600 μm, NA = 0.48) with a large numerical aperture (NA) by a convex lens. Finally, a spectrometer (Horiba Jobin Yvon iHR550) with an 1800 lines/mm grating and a charge coupled device (CCD) is used to analyze the emission spectrum. The measured laser emission was fitted with Lorentz distribution model to precisely determine the peak wavelength value (PWV).

1.4 References

[1] A. J. Cunningham, *Introduction to Bioanalytical Sensors*. New York, NY: Wiley, 1998.

[2] B. T. Cunningham and L. L. Laing, "Label-free detection of biomolecular interactions: Applications in proteomics and drug discovery," *Expert Review Proteomics,* vol. 3, pp. 271-281, 2006.

[3] B. T. Cunningham, P. Li, S. Schulz, B. Lin, C. Baird, J. Gerstenmaier, C. Genick, F. Wang, E. Fine, and L. Laing, "Label-free assays on the BIND system," *Journal of Biomolecular Screening,* vol. 9, pp. 481-490, 2004.

[4] A. L. Washburn, L. C. Gunn, and R. C. Bailey, "Label-free quantitation of a cancer biomarker in complex media using silicon photonic microring resonators," *Analytical Chemistry,* vol. 81, pp. 9499-9506, 2009.

[5] H. Zhu, I. M. White, J. D. Suter, P. S. Dale, and X. Fan, "Analysis of biomolecule detection with optofluidic ring resonator sensors," *Optics Express,* vol. 15, pp. 9139-9146, 2007.

[6] A. M. Armani, R. P. Kulkarni, S. E. Fraser, R. C. Flagan, and K. J. Vahala, "Label-free, single-molecule detection with optical microcavities," *Science,* vol. 317, p. 783, 2007.

[7] M. Lu, S. S. Choi, U. Irfan, and B. T. Cunningham, "Plastic distributed feedback laser biosensor," *Applied Physics Letters,* vol. 93, p. 111113, 2008.

[8] I. D. W. Samuel and G. A. Turnbull, "Organic Semiconductor Lasers," *Chemical Reviews,* vol. 107, pp. 1272-1295, 2007.

[9] G. Morthier, W. D'Oosterlinck, and K. Huybrechts, "All-optical flip-flops based on DFB laser diodes and DFB-arrays," *Journal of Materials Science: Materials in Electronics,* vol. 20, pp. 385-389, 2009.

[10] I. D. Block, L. L. Chan, and B. T. Cunningham, "Large-area submicron replica molding of porous low-k dielectric films and application to photonic crystal biosensor fabrication," *Microelectronic Engineering,* vol. 84, pp. 603-608, 2007.

[11] N. Ganesh, W. Zhang, P. C. Mathias, E. Chow, J. A. N. T. Soares, V. Malyarchuk, A. D. Smith, and B. T. Cunningham, "Enhanced fluorescence emission from quantum dots on a photonic crystal surface," *Nature Nanotechnology,* vol. 2, pp. 515-520, 2007.

[12] B. Park and M. Y. Han, "Organic light-emitting devices fabricated using a premetered coating process," *Optics Express,* vol. 17, pp. 21362-21369, 2009.

[13] M. Lu, S. Choi, C. J. Wagner, J. G. Eden, and B. T. Cunningham, "Label free biosensor incorporating a replica-molded, vertically emitting distributed feedback laser," *Applied Physics Letters,* vol. 92, p. 261502, 2008.

[14] J. Homola, S. S. Yee, and G. Gauglitz, "Surface plasmon resonance sensors: Review," *Sensors and Actuators B: Chemical,* vol. 54, pp. 3-15, 1999.

CHAPTER 2

LARGE AREA DFB LASER SENSOR FABRICATED BY NANO-REPLICA MOLDING AND HORIZONTAL DIPPING

The fabrication of visible wavelength ($564 < \lambda < 600$ nm) vertically emitting distributed feedback (DFB) lasers with a sub-wavelength grating fabricated by a replica molding process and an active polymer layer printed by a horizontal dipping process is reported. The combined techniques enable the organic DFB laser to be uniformly fabricated over large surface areas upon a flexible plastic substrate, with an approach that is compatible with roll-based manufacturing. The replica molding process is used to create a grating with a period of $\Lambda = 400$ nm and a depth of $d = 160$ nm, while the horizontal dipping method is used to create a dye-doped polymer waveguide layer with precisely controlled thickness. Using fixed grating period and depth, DFB laser output wavelength is controlled over a 40 nm range through manipulation of the waveguide layer thickness. The fabricated laser exhibits a linewidth of $\Delta\lambda = 0.15$ nm, threshold pump fluence of ~0.169 mJ-cm^{-2} at $\lambda = 532$ nm, and emission wavelength variation of 3.25 nm over a 10 cm^2 area. We demonstrate that the active area of the structure may be photolithographically patterned to create dense arrays of discrete DFB lasers.

2.1 Motivation and Project Description

Recently, solid state organic lasers have been successfully fabricated upon inexpensive substrates to reduce the manufacturing cost, with potential applications including communications, video display, and biosensors [1-3]. In addition to facilitating low manufacturing costs, fabrication upon flexible plastic substrates will enable lasers to be incorporated into curvilinear surfaces. Of the organic laser structures, the distributed feedback (DFB) laser has generated enthusiasm due to its wide wavelength range, compact structure, and compatibility with other thin film organic devices [4-7], with many recent efforts devoted to improving its performance and fabrication process while developing new applications [8, 9]. These efforts have yielded new benchmarks for operation lifetime, lasing threshold, and emission stability [10, 11].

Through selection of the DFB grating period, grating height, material refractive indices, dye material, and gain layer thickness, single-mode lasing output can be obtained with either horizontal or vertical emission for any desired wavelength from ultraviolet to near infrared [8, 11]. While many DFB lasers are designed to emit a single (static) wavelength, it is also possible to create DFB lasers whose output wavelength may be dynamically tuned [4-7]. One such example was recently demonstrated by Lu et al. [2, 3], in which incorporation of biomolecules on the surface of an organic vertically emitting DFB laser, designed so that a portion of the lasing mode extended into a liquid medium, resulted in an increase of the lasing wavelength. In general, many applications for which optically pumped organic DFB lasers have been demonstrated, including

sensing [2, 3] and spectroscopy [7], would benefit from a fabrication approach that provides a path toward inexpensive manufacturing.

One of the most efficient manufacturing paradigms currently available involves "roll-to-roll" processing, in which a flexible substrate material is unwound from a compact cylindrical spool so a series of fabrication processes can be performed in a continuous or stepwise manner, after which the substrate is wound upon a spool of "finished" material. Roll-based manufacturing is used for high volume, low cost, large surface area products, and can incorporate processes such as nanoreplica molding of quasi-three dimensional structures [12], dielectric thin film deposition, screen printing, and many others. After the roll-based processing is completed, individual parts may be cut from a roll using a die press or other automated cutting tool, and manipulated as individual pieces for assembly with other components. Due to the constraints of fabrication in a roll format, roll-based manufacturing is not compatible with the techniques (such as electron beam lithography) commonly used to obtain the submicron features of DFB lasers or techniques (such as spin-coating) that are used to obtain polymer films with precise submicron thickness. Roll-based fabrication upon plastic substrates is further constrained by the requirement not to exceed the softening temperature of the material, with a strong preference for processes that can be performed near room temperature.

In previous work, Cunningham and Laing [13] demonstrated a room temperature replica molding process for producing submicron grating features used for photonic crystal biosensors and photonic crystal enhanced-fluorescence substrates for biochemical

assays. The process for these devices involves roll-to-roll manufacturing of the grating structure, as well as roll-to-roll deposition of SiO_2 and TiO_2 sputtered dielectric thin films.

Recently, a novel process called “horizontal dipping” has been demonstrated as an effective method for producing thin polymer films used in organic light-emitting diodes (OLED) [14]. In horizontal dipping, a reservoir of coating fluid is maintained between the substrate and a horizontal metal rod placed ~1 mm above the substrate by capillary action. By drawing the substrate underneath the rod, a thin film is deposited upon the substrate, in which the resulting film thickness is accurately controlled by the dilution of the polymer within the coating solvent and by the velocity of the substrate as it passes under the rod. Because horizontal dipping is easily controlled, performed at room temperature, and requires no substrate rotation, it is an ideal process for creating the dye-doped polymer waveguide region of a DFB laser.

This chapter describes the uniform, large-area fabrication of an organic DFB laser structure on a flexible plastic substrate, for which the DFB grating is produced by nanoreplica molding and the dye-doped waveguide region is produced by horizontal dipping. We focus mainly upon characterization of the horizontal dipping process, and characterize the relationship between dipping speed and the thickness of the resulting polymer layer. Precise control and uniformity of the polymer waveguide layer is particularly important for the DFB laser, as a layer with thickness <515 nm is required to obtain single mode output, and the laser output wavelength is dependent upon the waveguide thickness. Control of the waveguide thickness provides a means for obtaining

any desired laser wavelength over a ~35 nm wavelength range, holding all other variables constant. Using a detection instrument that enables spatial mapping of the laser wavelength over a ~10 cm^2 surface area, the uniformity of the replica molding/horizontal dipping process is demonstrated. Finally, the horizontally dipped waveguide layer may be easily patterned by photolithography to create distinct, isolated regions of DFB laser. Although the application that motivates our research is the development of DFB laser biosensor surfaces for applications in life science research, pharmaceutical discovery, and diagnostic tests, the method presented here may be used to inexpensively fabricate any DFB laser structure for a broad range of applications.

2.2 DFB Laser Sensor Fabrication

A cross-sectional diagram of a representative vertically emitting organic DFB laser is shown in Fig. 1.2. The substrate is a flexible polyester (PET) film and the grating is formed in a layer of UV-curable polymer (UVCP) by a replica molding process. The corrugated UVCP layer functions as a distributed reflector and also as a cladding layer. Following the grating replication process, the grating surface is coated with a laser dye doped polymer layer using horizontal dipping process. This layer is responsible for light amplification and also serves as a waveguide providing light confinement. As indicated in Equation (1.2), the laser emission wavelength is linearly proportional to the effective index of the laser cavity, which depends on the thickness and refractive index of the wave guidance layer, the refractive index of the cladding layer and surrounding material. Therefore, single-mode DFB lasers operating in a wavelength range as wide as 35.51 nm

can be realized by precise control of the wave guidance layer thickness during the horizontal dipping process. The fabrication process is summarized schematically in Fig. 2.1.

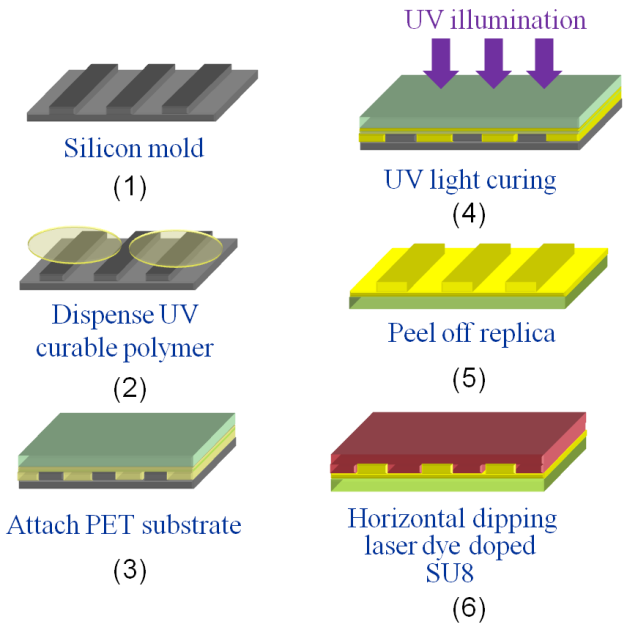

Fig. 2.1 Process flow diagrams for the solid state organic DFB laser.

2.2.1 Nano-replica molding

To perform nano-replica molding, a master mold with negative image of the sub-wavelength grating was produced by nano-imprint lithography on an 8 inch-diameter Si wafer [15, 16]. The patterned silicon wafer has a period of 400 nm, a duty cycle of 50%, and a depth of 160 nm. The silicon master mold was treated with Repel Silane (Amersham Biosciences) to facilitate mold separation. A small volume (~ 1 ml) of liquid UV-curable polymer (WR354, SSCP CO., LTD.) was dispensed onto the silicon master wafer surface. After attaching a PET sheet, the liquid UVCP was squeezed between the master mold and the PET substrate with a roller, enabling the UVCP to spread and fill

the grating uniformly. The UV-curing process takes place under high intensity UV lamp (Xenon) exposure for ~90 seconds at room temperature. After curing, the silicon mold and the replica of the grating are separated by peeling the PET substrate away from the silicon mold such that the cured polymer grating preferentially and permanently adheres to the PET substrate. The cured polymer film has a refractive index of 1.38 at 600 nm and a thickness around 5 μm.

2.2.2 Horizontal dipping process

The horizontal dipping process is capable of coating organic film over a large thickness range on various substrates. The horizontal dipping coating method is categorized as a pre-metered coating technique, which means the thickness of the coated film is determined by the process itself, unlike other coating techniques such as knife over roll coating [12], air knife coating [12] or metering rod coating, for which the thickness of the coated film is determined by an external process. Given a specific substrate and coating material combination, there are two ways to control the thickness. The first method is to adjust the spacing between the cylindrical barrier and the substrate, while the second method is to control the translation speed of the carrier stage. In the work reported here, the second method is adopted. The core component of the horizontal dipping setup is a stainless steel coating barrier (SUS Steel), which is a cylindrical rod with a radius of 0.25 inch. The coating barrier is mounted on a two-dimensional (x and z) translation stage. The vertical stage is used to adjust the barrier height, h_0, with respect to the substrate surface. A motorized horizontal stage (SGSP 26-150, Optosigma) moves

the coating barrier over the grating substrate with speed controlled by a programmable motor controller (SHOT-602, Optosigma).

Before the dipping process, the active polymer layer was prepared by mixing a 5 mg/ml solution of Rhodamine 590 dye (Exciton) in CH_2Cl_2 with SU-8 (5.0 wt %; Microchem) to a volume percentage of 10%. This mixture was sonicated for improved homogenization. The dye doped polymer solution was injected into the gap between the barrier and the substrate by a syringe. The solution spread in the gap due to capillary effect and formed a downstream meniscus [12, 14]. During the horizontal dipping process, the substrate was held horizontally by a vacuum chuck and the barrier translated smoothly at a preset speed, leaving a thin film of the dye doped solution on the grating substrate. After the dipping process, the coated device was soft baked on a 95 °C hotplate for 1 min to remove the solvent. After that, the SU-8 film was photopolymerized by exposing to UV radiation (365 nm lamp source) with exposure dose of 100 mJ cm^{-2}, and subsequently hard baked on a 95 °C hot plate for 2 min.

Using SU-8 with a viscosity of 7.5 cSt, the barrier height and dragging speed affect the coating thickness which, in turn, determines the stimulated emission wavelength. The relationship between the film thickness and the dragging speed was studied using an atomic force microscope (AFM) (Digital Instruments Dimension 3000 Atomic Force Microscope, Veeco) and an optical interferometry profiler (Veeco NT1000 optical profiler, Veeco). In addition, since the thickness of the gain layer is closely related to the stimulated emission wavelength, by measuring the spatial distribution of the laser emission spectrum, we can also map out the spatial variation of the refractive

index on top of the laser surface, so as to characterize the uniformity or surface morphology of the device.

2.2.3 Active layer pattern process

For some applications, it will be interesting if the emission region can be patterned. Using SU-8 as the laser dye host allows us to easily pattern the light emission area in any shapes with conventional photolithography. As mentioned above, after the device was soft baked on a 95 °C hotplate for 1 min to remove the solvent, the device was photopolymerized by exposing to UV radiation (365 nm lamp source) with a predefined photomask. Specially, we designed a photomask having a pattern of a Chinese character "中" which occupies a 1mm×1mm area with a feature size of 125 μm. The exposed film was post-baked at 95 °C for 120 seconds and the unexposed area was removed by the developing process, resulting in a patterned area with a negative image of the pattern mask.

Previous work has shown that the nanoreplica molding process is capable of reproducing sub-wavelength grating structures over large surface areas [3], and implementation of a roll-to-roll process for high volume manufacturing. We envision that the horizontal dipping process can be implemented as a process that can be performed in a roll-to-roll manner upon replica-molded grating structures either on a separate piece of manufacturing equipment, or integrated within a machine that can perform both processes.

2.3 Device Characterization

The experimental setup as presented in Fig 1.3 in Chapter 1 was utilized to analyze and evaluate the device performance.

2.3.1 Film thickness

For the horizontal dipping process, the coating polymer is categorized as a Newtonian liquid which is usually characterized by its viscosity, density, and surface tension [12]. A downstream meniscus shape will form after the solution is fed into the gap between the stainless steel barrier and the grating surface. The relationship between the film thickness and the radius of the curvature of the downstream meniscus is given by

$$t_w = 1.34\left(\frac{\mu U}{\sigma}\right)^{2/3} \cdot R_d \qquad (2.1)$$

where R_d represents the radius of curvature of the downstream meniscus, μ and σ represent the viscosity and surface tension of the coating solution, respectively, and U is the carrying speed [12, 14]. During the coating process, the gap between the stainless steel barrier and the grating surface was kept at 0.9 mm and the translation velocity of the barrier was adjusted from 0.01 cm/s to 0.8 cm/s. The resulting gain layer thickness ranged from 234.0 nm to more than 3.1 μm, as shown in Fig. 2.2. With the lowest translation speed of 0.01 cm/s, a film thickness around 234 nm was achieved. The film thickness was measured both by atomic force microscope (AFM) (Digital Instruments Dimension 3000 Atomic Force Microscope, Veeco) and optical surface profiler (Veeco NT1000 optical profiler, Veeco). The measurement results are compared to the theoretical prediction which corresponds to the red curve in Fig. 2.2.

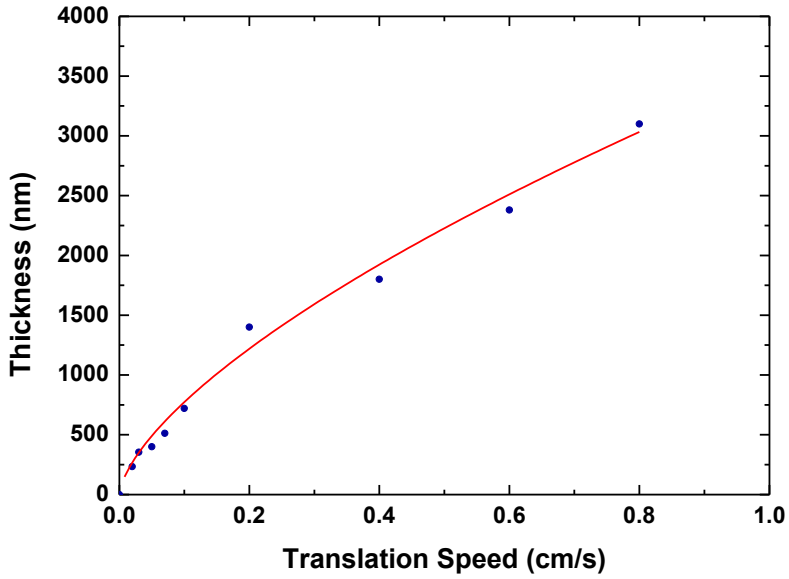

Fig. 2.2 Relationship between the translation speed of the carrier stage and the guidance layer thickness: the translation speed ranges from 0.01 cm/s to 0.8 cm/s and the corresponding film thickness ranges from 234 nm to ~3.1 μm.

2.3.2 DFB laser performance

Another advantage of this fabrication strategy is the wide tunability of the lasing emission wavelength. As mentioned in the device design section, the lasing wavelength can be tuned within the emission spectral region of gain by modifying the effective refractive index via control of the thickness of the wave guidance layer. The stimulated emission wavelengths of devices with different guidance layer thicknesses were measured and are shown in Fig. 2.3. Since the guidance layer has a larger refractive index than the superstrate media and the substrate layer, an increase of the thickness of the guidance layer will introduce a red-shift of the lasing emission wavelength. The relationship between the guidance layer thickness and the stimulated emission wavelength is depicted in the inset plot. Single-mode emissions were observed when the

guidance layer thickness was within a range of 234 nm to 510 nm. When a much thicker guidance layer was employed, the laser began to display multimode emission, as shown in the top left inset picture.

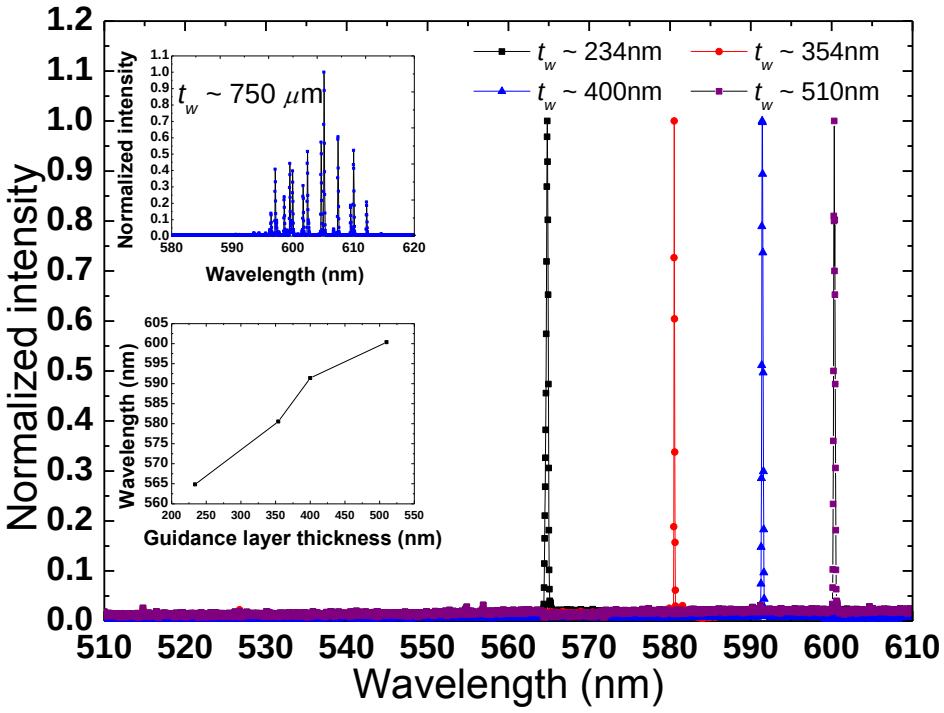

Fig. 2.3 Stimulated emission spectrum of devices with different guidance layer thicknesses. The fabricated lasers exhibit a linewidth of $\Delta\lambda = 0.15$ nm, threshold pump fluence 0.169 mJ-cm^{-2} at $\lambda = 532$ nm. The top left inset picture shows multiple-mode emission when the guidance layer thickness is ~750 μm. The bottom left inset plot shows the relationship between the laser emission wavelength and the guidance layer thickness.

2.3.3 Film thickness uniformity

Due to the relationship between the thickness of the guidance layer and the laser emission wavelength, the uniformity of the device can be investigated by measurement of the spatial distribution of stimulated emission wavelengths. The measurement results are shown in Fig. 2.4. The laser emission wavelength measurement was first performed in a line-by-line manner with 2 mm spacing between adjacent sampling spots on a device

having an area of 50 mm × 20 mm, as shown in the top of Fig. 2.4. The range of the PWV variation is 3.15 nm, which indicates a variation range of ~36 nm of the guidance layer thickness according to rigorous coupled wave analysis (RCWA) simulations of the device structure (simulation results not shown). The standard deviation of PWV is 0.514 nm, resulting in a coefficient of variation of CV = 0.087%. To characterize the uniformity with a finer spatial scale over a small surface area, a zoomed in measurement was performed in a single 2 mm × 2 mm square, with 125 μm spacing between adjacent sampling spots. As shown in the bottom of Fig. 2.4, the PWV range was $\Delta\lambda$ = 0.481 nm, with a standard deviation of 0.129 nm and a coefficient of variation of CV = 0.022% The measured standard deviation of DFB output wavelength corresponds to only ~1.57 nm standard deviation of the guidance layer thickness over a 4 mm^2 area. These results were further verified by an AFM measurement.

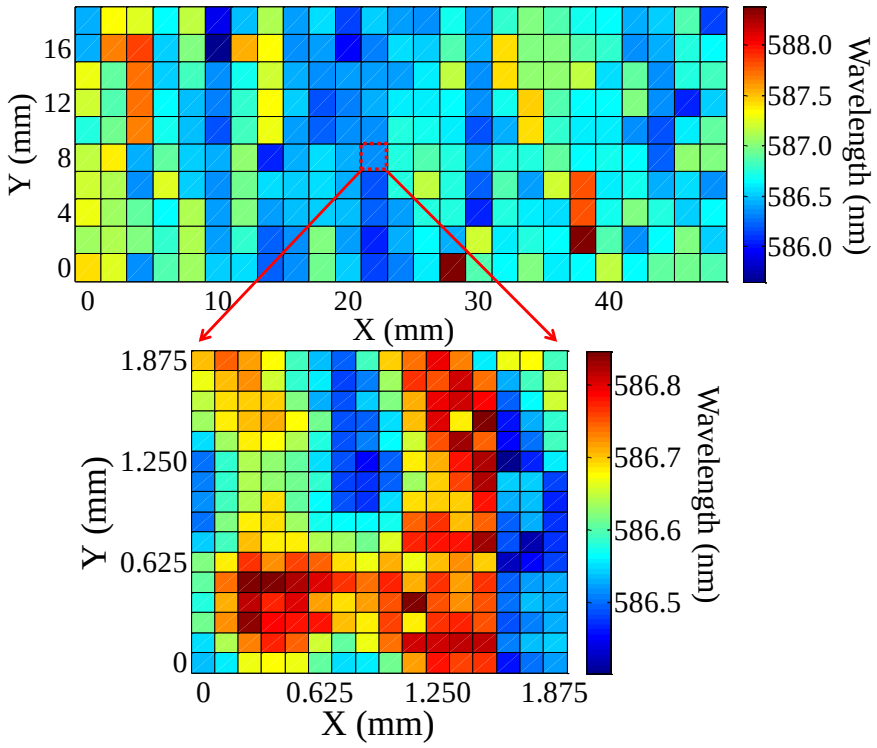

Fig. 2.4 Spatial distribution of the laser emission wavelength. The top picture illustrates a map of laser emission wavelength over a 5 cm × 2 cm area. The bottom picture shows a zoomed-in perspective of the lasing wavelength distribution within a single grip with a 2 mm × 2 mm area.

2.3.4 Emission image of patterned DFB laser

In some applications, it is desirable for the laser light source to be patterned. For example, for our application for creating DFB laser biosensors, it is often desirable to create discrete regions of DFB laser surface that can be functionalized with different capture molecules for creating an array of small sensors that can be probed individually. Patterning by photolithography is an established fabrication process involving simple steps, including photoresist (PR) coating, PR baking, exposure, developing, material etching and PR stripping. Devices made by the method described in this work can be easily patterned using photolithography, while still in a roll-based format because the horizontal-dipped layer of the dye-doped SU-8 is photosensitive.

Figure 2.5 shows the spatial laser emission profile of a device with a patterned SU-8 layer, using the process described above, in which the mask was created by printing ink on a transparent plastic sheet with a laser printer. Since the laser-printed pattern has a feature resolution of 125 μm, the spatial resolution between the adjacent pumping spot was chosen to be 12.5 μm to satisfy the Nyquist sampling frequency. In Fig. 2.5, regions that do not lase are assigned a wavelength of 0 nm, and are displayed in black. The spatial distribution of the stimulated emission wavelength along the horizontal direction is also shown. The variation is within a $\Delta\lambda$ = 0.14 nm range.

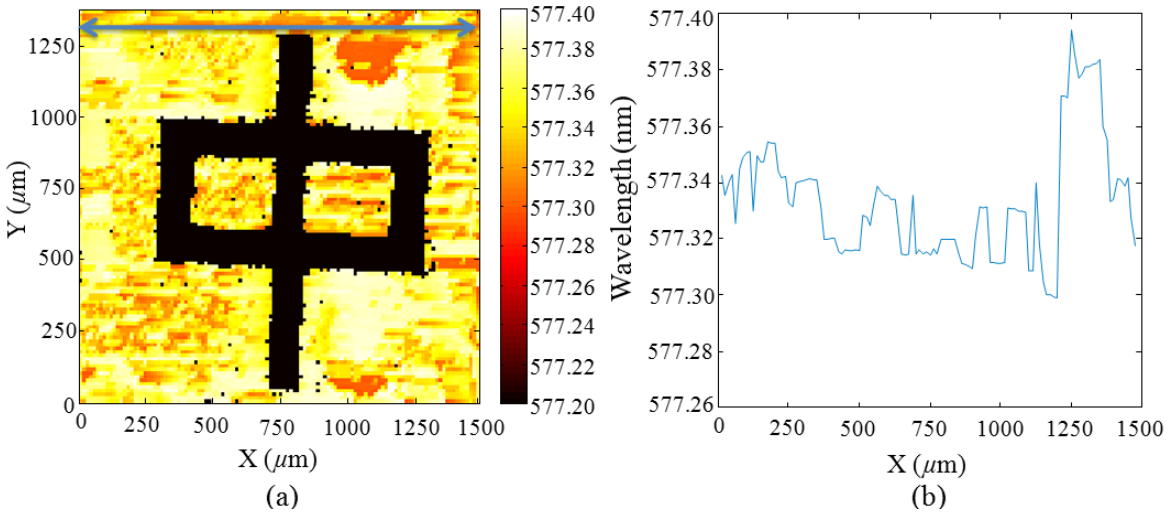

Fig. 2.5 Emission characteristics of a patterned DFB laser. (a) The stimulated emission image of a patterned DFB laser: The black part with a pattern “中” indicates the dumb region where the gain layer has been removed. So the laser does not lase there, while the laser works normally in the complementary region. The spatial resolution of the image is 12.5 μm, and the feature size of the pattern is 125 μm. (b) The spatial distribution of the stimulated emission wavelength across a horizontal line in (a): The variation of the lasing emission is within a 0.14 nm range, while the lasing wavelength difference between adjacent spots is less than 0.01 nm.

2.4 Conclusion

A fabrication method that combines nanoreplica molding and horizontal dipping processes has been developed for organic DFB lasers upon flexible plastic substrates. The spatially corrugated surface can be produced inexpensively and in virtually any periodicity upon a plastic substrate by the nano-replica molding method. The subsequent horizontal dipping process allows uniform coating of dye doped polymer active layer onto the grating surface at desired thickness ranging from 234.0 nm to 3.1 μm. Lasing from the polymer-based DFB structure, having a replicated $\Lambda = 400$ nm polymer grating and a Rhodamine 590 doped SU-8 active medium, has been demonstrated and characterized. The laser emission wavelength can be controlled in the $\lambda = 564.82$ to 600.33 nm wavelength range. The tested DFB laser exhibits a linewidth of $\Delta\lambda = 0.15$ nm, a threshold pump fluence ~0.169 mJ-cm^{-2} at $\lambda = 532.00$ nm, and emission wavelength variations as small as 3.15 nm over a 10 cm^2 area. From this example of a plastic DFB laser, it is clear that the developed fabrication method has the capability of producing organic DFB laser and organic DFB laser arrays for a wide range of wavelengths.

2.5 References

[1] G. Morthier, W. D'Oosterlinck, and K. Huybrechts, "All-optical flip-flops based on DFB laser diodes and DFB-arrays," *Journal of Materials Science: Materials in Electronics,* vol. 20, pp. 385-389, 2009.

[2] M. Lu, S. S. Choi, C. J. Wagner, J. G. Eden, and B. T. Cunningham, "Label free biosensor incorporating a replica-molded, vertically emitting distributed feedback laser," *Applied Physics Letters,* vol. 92, p. 261502, 2008.

[3] M. Lu, S. S. Choi, U. Irfan, and B. T. Cunningham, "Plastic distributed feedback laser biosensor," *Applied Physics Letters,* vol. 93, p. 111113, 2008.

[4] N. Tsutsumi, A. Fujihara, and D. Hayashi, "Tunable distributed feedback lasing with a threshold inthe nanojoule range in an organic guest-host polymeric waveguide," *Applied Optics,* vol. 45, pp. 5748-5751, 2006.

[5] T. Riedl, T. Rabe, H.-H. Johannes, W. Kowalsky, J. Wang, T. Weimann, P. Hinze, B. Nehls, T. Farrell, and U. Scherf, "Tunable organic thin-film laser pumped by an inorganic violet diode laser," *Applied Physics Letters,* vol. 88, p. 241116, 2006.

[6] D. Schneider, T. Rabe, T. Riedl, T. Dobbertin, M. Kroger, E. Becker, H.-H. Johannes, W. Kowalsky, T. Weimann, J. Wang, and P. Hinze, "Ultrawide tuning range in doped organic solid-state lasers," *Applied Physics Letters,* vol. 85, pp. 1886-1888, 2004.

[7] L. Xue, S. R. J. Brueck, and R. Kaspi, "Widely tunable distributed-feedback lasers with chirped gratings," *Applied Physics Letters,* vol. 94, p. 161102, 2009.

[8] P. D. Carro, A. Camposeo, R. Stabile, E. Mele, L. Persano, R. Cingolani, and D. Pisignano, "Near-infrared imprinted distributed feedback lasers," *Applied Physics Letters,* vol. 89, p. 201105, 2006.

[9] D. Pisignano, L. Persano, P. Visconti, R. Cingolani, G. Gigli, G. Barbarella, and L. Favaretto, "Oligomer-based organic distributed feedback lasers by room-temperature nanoimprint lithography," *Applied Physics Letters,* vol. 83, pp. 2545-2547, 2003.

[10] R. Harbers, P. Strasser, D. Caimi, R. F. Mahrt, N. Moll, B. J. Offrein, D. Erni, W. Bachtold, and U. Scherf, "Enhanced feedback in organic photonic-crystal lasers," *Applied Physics Letters,* vol. 87, p. 151121, 2005.

[11] Z. Li, Z. Zhang, T. Emery, A. Scherer, and D. Psaltis, "Single mode optofluidic distributed feedback dye laser," *Optics Express,* vol. 14, pp. 696-701, 2006.

[12] F. C. Krebs, "Polymer solar cell modules prepared using roll-to-roll methods: Knife-over-edge coating, slot-die coating and screen printing," *Solar Energy Materials and Solar Cells,* vol. 93, pp. 465-475, 2009.

[13] B. T. Cunningham and L. Laing, "Microplate-based, label-free detection of biomolecular interactions: Applications in proteomics," *Expert Review of Proteomics,* vol. 3, pp. 271-281, Jun 2006.

[14] B. Park and M. Y. Han, "Organic light-emitting devices fabricated using a premetered coating process," *Optics Express,* vol. 17, pp. 21362-21369, 2009.

[15] S. Y. Chou, P. R. Krauss, and P. J. Renstrom, "Nanoimprint lithography," *Journal of Vacuum Science & Technology B,* vol. 14, pp. 4129-4133, 1996.

[16] S. Y. Chou, P. R. Krauss, and P. J. Renstrom, "Imprint lithography with 25-nanometer resolution," *Science,* vol. 272, pp. 85-87, 1996.

CHAPTER 3

LASER THRESHOLD REDUCTION BY RESONANT OPTICAL PUMPING

This chapter shows that the stimulated emission threshold from a distributed feedback (DFB) structure, based upon a second order grating in a dye-doped polymer, has been efficiently reduced by implementing a resonant optical pumping scheme. The proposed scheme couples the excitation laser light into a resonant mode and takes the advantage of the intensified electromagnetic field. For a Bragg grating having a periodicity of 400 nm, a Rhodamine 590 doped polymer laser operates at 590 nm and concurrently supports a resonance mode at 532 nm, which is the excitation laser wavelength. Pumped under the resonance condition, the DFB laser exhibits 25-fold threshold reduction. In addition, the resonant optical pumping technique also enhances the light conversion efficiency by a factor of 23. This technique improves performance of organic DFB lasers.

3.1 Motivation and Project Description

Many methods have been used to lower the lasing threshold [1-6]. One of the strategies is to use a microcavity. A ‘‘zero-threshold’’ laser was demonstrated for dye solution in a planar microcavity half the length of the resonant wavelength. The stimulated as well as spontaneous emission rate in the cavity is proportional to the mode density for a

final photon state in the cavity, and is inversely proportional to the mode volume. At the lasing threshold, stimulated gain of the active material is equal to the total loss including the intrinsic cavity loss and other extrinsic loss. This equality leads to the expression for lasing. Besides the optical cavity, the gain material property is also important. Laser threshold directly benefits from using more efficient gain material. Another strategy to reduce the lasing threshold is to reduce the nonradioactive loss in the gain material [1]. Alternatively, this chapter describes a novel method, resonant optical pumping, to lower the lasing threshold of a vertically emitting DFB laser and improve the quantum efficiency of the laser at the same time. The resonant pumping technique utilizes the strongly intensified near optical field caused by the resonant mode supported by the DFB laser itself.

Since the demonstrations (in 1971) of lasing in which optical feedback was provided by a corrugated, periodic refractive index structure, organic dyes have offered a versatile gain medium for the evaluation of integrated resonator designs, waveguide configurations and microlaser fabrication techniques [7]. DFB structures are generally preferred for solid state dye lasers, principally because of end-on or out-of-plane emission, broad tunability, and narrow linewidth, are available with DFB-based oscillators. The DFB dye lasers were usually made by either periodic gain modulation or periodic refractive index modulation. A drawback of current organic DFB dye laser designs, however, is their high threshold which usually necessitates a nano-second pulse laser as the pumping light source.

The one-dimensional photonic crystal optical cavity of a surface-emitting DFB laser concurrently supports resonant modes at both stimulated emission wavelength and excitation laser wavelength. Such a laser takes advantage of the evanescent field that has increased local energy density with respect to the incident light. The intensified evanescent field strongly excites fluorophores located inside the laser cavity, which results in enhanced fluorescent emission from the fluorophores. Previous publications have demonstrated the use of photonic crystal structures with the resonant mode spectrally overlapping the laser wavelength, to excite fluorescent dyes [8].

3.2 Enhanced Field

A cross-sectional diagram (not to scale) of the DFB laser is shown in Fig. 1.2 in Chapter 1. The DFB laser cavity possesses a 1D photonic crystal structure. Such a structure is capable of concurrently supporting different resonant modes including the laser emission mode as well as the optical pumping mode. Illuminating at a particular wavelength and incident angle, the incident light could be coupled into the cavity as a resonant mode by satisfying the phase matching condition [9]. The specific incident angle is defined as the resonant pumping angle for that particular wavelength. The phase matching condition for in-coupling light to a resonant mode is given by

$$k_0 \sin(\theta_0) \pm m\frac{2\pi}{\Lambda} = \frac{2\pi}{\lambda} n_{eff} \tag{3.1}$$

where k_0 is the free-space wave number, θ_0 is the resonance angle measured from the normal, m is the diffraction order, Λ is the grating period, λ is the resonance wavelength,

and n_{eff} is the effective index of the resonant mode. Equation (3.1) shows how one can vary the illumination angle, wavelength, or both to excite a resonance.

The scheme applied here is to couple the pumping light into a resonant mode by illuminating at the resonant angle. The energy at resonance is confined in the laser cavity. Such a compression of mode volume leads to a strongly intensified local electromagnetic field. Due to the spatial overlap between the resonant mode and the organic laser dye, the emission of the dye is also strongly enhanced, leading to a reduction of lasing threshold and an improvement of the slope efficiency. The resonant pumping angle and electric field intensity profile were calculated based on rigorous coupled wave analysis (RCWA). The RCWA algorithm, also known as the Fourier modal method, is a computational electromagnetic method to study periodic structures such as waveguide resonant grating, diffraction optical element, and photonic bandgap crystal [10]. The RCWA algorithm first transfers the spatial periodic dielectric distribution into the summation of a series of Fourier harmonics. The electromagnetic fields within the computation domain are correspondingly written as the summation of Fourier harmonics with unknown coefficients. By enforcing the continuity conditions at different material interfaces, the algorithm generates an array of equations derived from Maxwell's equations. The unknown coefficients for individual Fourier harmonics are subsequently calculated by numerically solving the equations. As a postprocess, the light diffraction, reflection, transmission efficiency and electric field distribution can be calculated .

Figure 3.1 illustrates the normalized distribution of the electric field intensity of the pumping light under resonant pumping and non-resonant pumping. In both plots, the sensor's top horizontal surface is located at z = 400 and is indicated by the upper horizontal white line. As shown in Fig. 3.1 (a), the electromagnetic field of the pump light wave is trapped and enhanced inside the laser cavity and has a significant overlap with the gain material when illuminated from the resonant pump angle. The field intensity is trivial outside the cavity but maximized inside the gain material, and is ~400× higher than the normalized pump light intensity. While under non-resonant pumping, as illustrated by Fig. 3.2 (b), the field of the pump light does not efficiently overlap with the gain material. In this situation, the maximum of the near-field intensity is only ~5× higher than that of the pump light and is located outside of the gain layer.

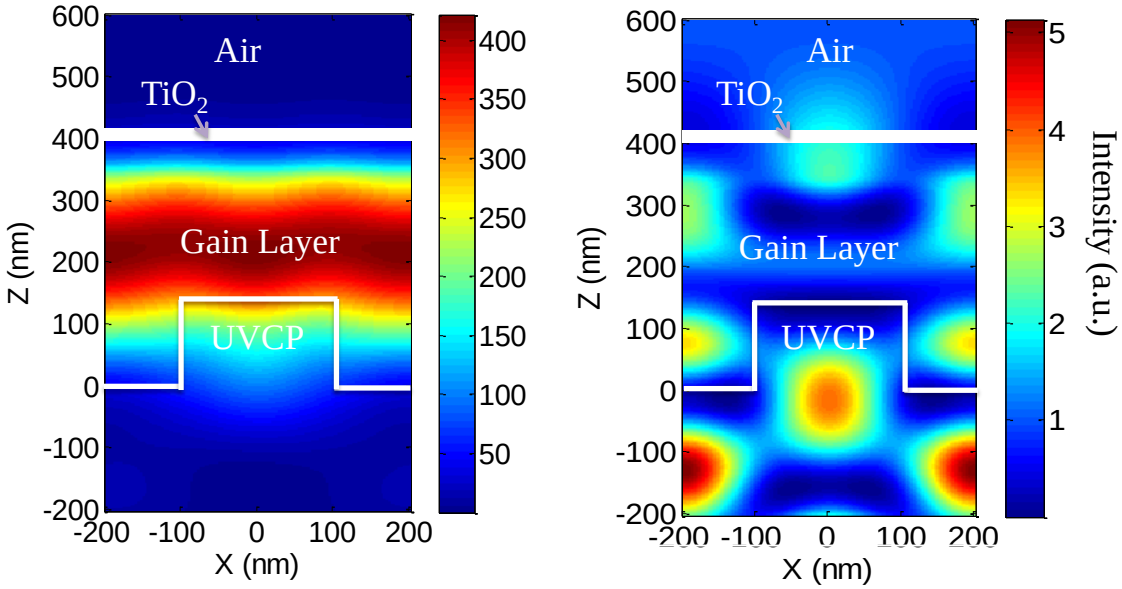

Fig. 3.1 Near-field intensity calculation. Electric field intensity profile calculated using RCWA for the TE pumping mode at λ = 532 nm under resonant pumping condition (a) and non-resonant pumping condition (b). Note different color bar scales are used.

3.3 Experiment Setup

The device was prepared in the way described in Chapter 2, but the experiment setup differed from the setup described in Chapter 1. During the experiment investigating the dependency of the laser threshold and the quantum efficiency on the pumping angle, a frequency-doubled, Q-switched Nd: YAG pulse laser (λp = 532 nm, yttrium aluminum garnet) with pulse duration of 10 ns at a repetition rate of 1 Hz was used as the light source. The excitation spot size and pump fluence were controlled by an adjustable pinhole and a continuous variable neutral density filter (OD 0-4.0). The DFB laser emission was normal to the device surface and was coupled by a convex lens into a step index multimode fiber with high numerical aperture (d = 600 μm, NA = 0.48). Because the one-dimensional grating DFB resonator only provides confinement perpendicular to grating axis, the beam highly diverges along the direction parallel to the grating axis. A fiber cable with a numerical angle (NA) of 0.5 was utilized to account for the high divergence of the DFB laser output. Then the laser output was analyzed by a spectrometer (HR4000 Ocean Optics) with a resolution of 0.12 nm. In order to ensure exciting at the same location, the device was placed on a rotation stage with the device surface overlapping the rotation axis, and the pumping light was controlled to pass through the rotation axis at a right angle. The same setup was used to investigate the laser emission intensity as a function of the pumping angle. A CW Nd: YAG laser was utilized as the excitation source in the experiment measuring the absorption coefficients when pumped at different angles. The incident light power reflected light power and

transmitted light power were measured using a Si photodiode based power and energy meter (PM320E, Thorlabs).

3.4 Results

3.4.1 Band diagram

The photonic band diagram of the device was measured by illuminating the device with collimated white light and the transmitted spectrum was collected and analyzed with a spectrometer (USB 2000, Ocean Optics) as a function of the incident angle. For the measurement, an angular step size of 0.25˚ was used. The consequent band diagram is shown in Fig. 3.2, in which the resonant pumping and laser emission can be identified. As highlighted in Fig. 3.2, a resonance for 532 nm is at 9.13°.

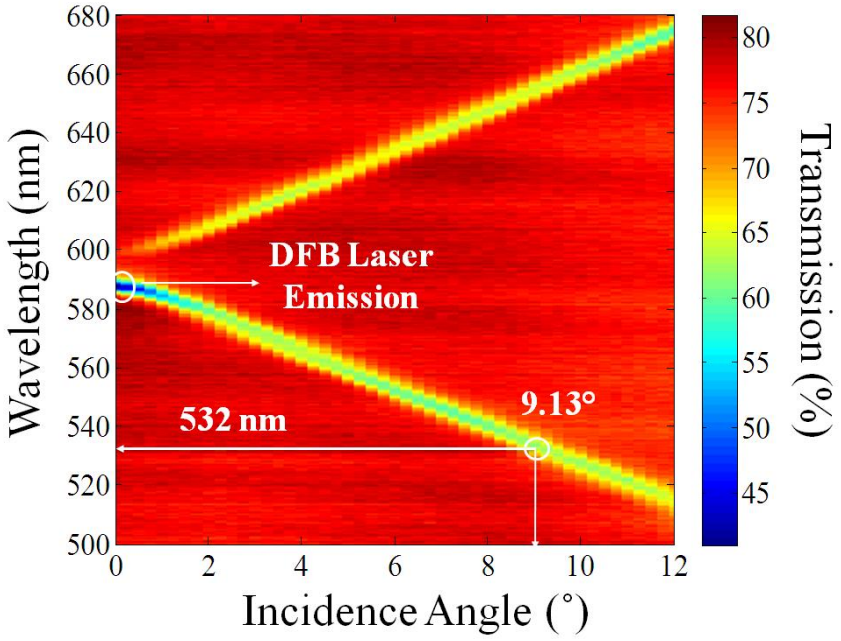

Fig. 3.2 Photonic band diagram of the DFB laser. Measured photonic dispersion of the resonant modes. The experimentally obtained data suggests that the pumping light at λ = 532 nm couples to resonant mode by following the photonic dispersion.

3.4.2 Reduce threshold and improved quantum efficiency

The reduced lasing threshold and improved slope efficiency resulting from resonant pumping were investigated through the measurement of the laser emission output under different excitation angles. Measurement results are shown in Fig. 3.3. The result exhibits a threshold of 8.55 μJ/mm^2 when the pumping light is normal to the laser surface, but a threshold of 0.34 μJ/mm^2 under resonant optical pumping. The result demonstrates that the application of a resonant pumping scheme results in a 25-fold reduction of the lasing threshold. At the same time, when compared to the off-resonant pumping, the slope efficiency was also improved by 23-fold. In addition, when the pumping was not precisely on resonance, but 0.05˚- 0.1˚ off, a clear reduction of the lasing threshold and an improvement of the slope efficiency were still observed, as

shown in the other two curves in Fig. 3.4. This is also expected from the intensified electrical field effect.

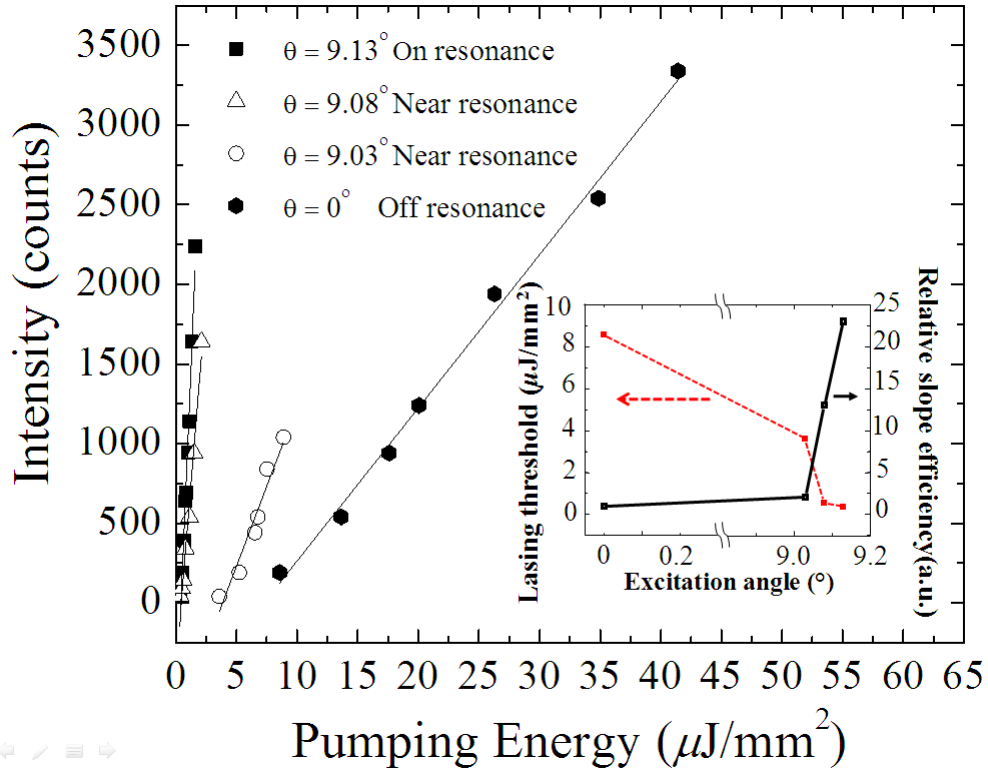

Fig. 3.3 Emission characteristics of a surface-emitting DFB laser in terms of the pumping angle. The inset picture depicts the lasing threshold and the slope efficiency as a function of the pumping angle. Threshold energies of ~ 0.34 μJ/mm^2, 0.55 μJ/mm^2, 3.59 μJ/mm^2, and 8.55 μJ/mm^2 were found for excitations from 9.13° (on resonance), 9.08° (near resonance), 9.03° (near resonance) and 0° (off resonance), using a linear least-squares fit to the experimentally obtained data. Fitting results indicate a 25× reduction in the threshold energy for lasing when pumped at the resonance angle (9.13°) compared to the case without using resonance (at 0°). Meanwhile, the slope efficiency is enhanced by 23× at resonance, according to the linear fitting.

3.4.3 Absorption efficiency vs. pumping angle

The relationship between the absorption efficiency and the pumping angle has also been investigated with measurement results shown in Fig. 3.4. A CW Nd: YAG laser was utilized as the excitation source during this experiment. Under resonant pumping, the absorption efficiency was maximized and was ~31.65%, while at normal incidence, the

absorption efficiency was only ~1.30% (not shown in Fig. 3.4). Therefore, the absorption efficiency could be increased by ~23× simply by implementing resonant pumping without changing the device configuration. Additionally, the curve characterizing the relationship between the absorption and the pumping angle agrees well with the relationship observed between the laser emission intensity and the pump incident angle. This agreement indicates that the reduced lasing threshold and improved slope efficiency result from the increased pumping energy absorption. This increased energy absorption will enhance the resonant electromagnetic field inside the gain layer, which in turn will dramatically decrease the laser pump threshold power and improve the slope efficiency.

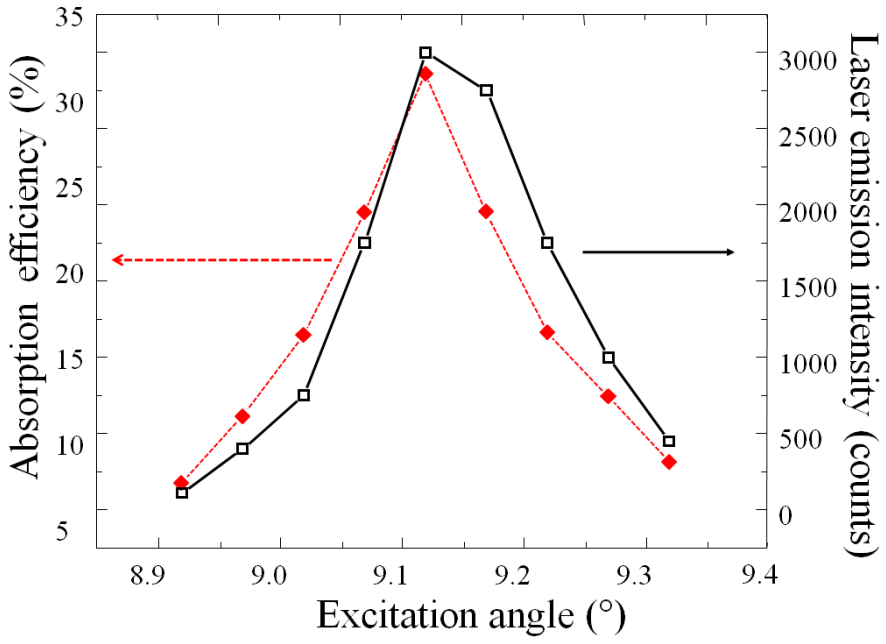

Fig. 3.4 Absorption efficiency and laser output versus the pumping angle. Both the absorption efficiency of the pumping energy and the laser output peak at the resonant excitation angle (9.13°) drop in the same manner as the pumping light shifts away from the resonant incident angle. This agreement indicates that it is the increased pumping energy absorption that results in the reduced lasing threshold and the improved slope efficiency.

3.5 Conclusion

In summary, optimized operation of a laser usually involves a tradeoff between high slope efficiency and low threshold pump power. This chapter describes a novel resonant optical pumping (ROP) technique that helps to solve this contradiction. As a demonstration, the ROP technique was applied to a surface-emitting distributed feedback laser, and resulted in a 25× reduction in threshold energy and a 23× enhancement in slope efficiency. This technique can be applied to any laser cavity with co-existing modes at both lasing and pump wavelength to reduce the pump threshold and to increase the slope efficiency.

3.6 References

[1] R. Harbers, P. Strasser, D. Caimi, R. F. Mahrt, N. Moll, B. J. Offrein, D. Erni, W. Bachtold, and U. Scherf, "Enhanced feedback in organic photonic-crystal lasers," *Applied Physics Letters,* vol. 87, p. 151121, 2005.

[2] W. Song, A. E. Vasdekis, Z. Li, and D. Psaltis, "Low-order distributed feedback optofluidic dye laser with reduced threshold," *Applied Physics Letters,* vol. 94, p. 051117, 2009.

[3] G. Tsiminis, Y. Wang, P. E. Shaw, A. L. Kanibolotsky, I. F. Perepichka, M. D. Dawson, P. J. Skabara, G. A. Turnbull, and I. D. W. Samuel, "Low-threshold organic laser based on an oligofluorene truxene with low optical losses," *Applied Physics Letters,* vol. 94, p. 243304, 2009.

[4] C. Karnutsch, C. Gyrtner, V. Haug, U. Lemmer, T. Farrell, B. S. Nehls, U. Scherf, J. Wang, T. Weimann, G. Heliotis, C. Pflumm, J. C. deMello, and D. D. C. Bradley, "Low threshold blue conjugated polymer lasers with first- and second-order distributed feedback," *Applied Physics Letters,* vol. 89, p. 201108, 2006.

[5] D. Schneider, T. Rabe, T. Riedl, T. Dobbertin, M. Kroger, E. Becker, H.-H. Johannes, W. Kowalsky, T. Weimann, J. Wang, and P. Hinze, "Laser threshold

reduction in an all-spiro guest--host system," *Applied Physics Letters,* vol. 85, pp. 1659-1661, 2004.

[6] M. Ichikawa, Y. Tanaka, N. Suganuma, T. Koyama, and Y. Taniguchi, "Low-threshold photopumped distributed feedback plastic laser made by replica molding," *Japanese Journal of Applied Physics Part 1-Regular Papers Short Notes & Review Papers,* vol. 42, pp. 5590-5593, 2003.

[7] C. V. Shank, Bjorkhol.Je, and H. Kogelnik, "Tunable Distributed-Feedback Dye Laser," *Applied Physics Letters,* vol. 18, pp. 395-398, 1971.

[8] N. Ganesh, W. Zhang, P. C. Mathias, E. Chow, J. A. N. T. Soares, V. Malyarchuk, A. D. Smith, and B. T. Cunningham, "Enhanced fluorescence emission from quantum dots on a photonic crystal surface," *Nature Nanotechnology,* vol. 2, pp. 515-520, 2007.

[9] D. Rosenblatt, A. Sharon, and A. A. Friesem, "Resonant grating waveguide structures," *Quantum Electronics, IEEE Journal of,* vol. 33, pp. 2038-2059, 1997.

[10] N. P. van der Aa and R. M. M. Mattheij, "Computing shape parameter sensitivity of the field of one-dimensional surface-relief gratings by using an analytical approach based on RCWA," *Journal of the Optical Society of America A,* vol. 24, pp. 2692-2700, 2007.

CHAPTER 4

SURFACE SENSITIVITY ENHANCED DFB LASER BIOSENSOR

A dielectric nanorod structure is used to enhance the label-free detection sensitivity of a vertically emitting distributed feedback laser biosensor (DFBLB). The device comprises a replica molded plastic grating that is subsequently coated with a dye-doped polymer layer and a TiO_2 nanorod layer produced by the glancing angle deposition technique. The DFBLB emission wavelength is modulated by the adsorption of biomolecules, whose greater dielectric permittivity with respect to the surrounding liquid media will increase the laser wavelength in proportion to the density of surface-adsorbed biomaterial. The nanorod layer provides greater surface area than a solid dielectric thin film, resulting in the ability to incorporate a greater number of molecules. The detection of a monolayer of protein polymer poly (Lys, Phe) is used to demonstrate that a 90 nm TiO_2 nanorod structure improves the detection sensitivity by a factor of 6.6 compared to an identical sensor with a nonporous TiO_2 surface.

4.1 Motivation and Project Description

In previous work, Lu et al. have demonstrated DFBLB sensors that incorporate a thin solid film of TiO_2 as the uppermost surface, where a 40-80 nm thick layer of TiO_2 serves to bias the resonant mode to reside more fully within the liquid media in contact with the

DFBLB surface, thus providing a strong dependency of the emission wavelength on the density of adsorbed biomolecules [1] .

Here, a nanostructured high refractive index layer of TiO_2 nanorods is applied to replace the thin solid film of TiO_2. It is shown that the use of the nanostructured film results in a three-dimensional volume overlap between the DFBLB resonant mode and the region in which biomolecule adsorption can occur. This modification in device design results in a ~6.6× increase in detection sensitivity, while at the same time maintaining a narrow spectral output, with cavity quality factor Q = 25,600. The TiO_2 nanorod structure was deposited by e-beam evaporation using the glancing angle deposition (GLAD) method in which the incident material flux is provided at an oblique angle to the device surface.

4.2 Glancing Angle Deposition

The TiO_2 nanorod layer is deposited on top of the SU-8/dye layer by the GLAD technique. GLAD is a physical vapor deposition process where the deposition flux is incident onto a substrate with a large angle with respect to the surface normal [2]. GLAD can be used to produce columnar structures through the effect of shadowing during film growth. Since GLAD is a physical vapor deposition technique, it has many advantages in terms of controlling the growth of nanostructured thin films: (1) It can produce nano-column arrays naturally. (2) The porosity of the film can be controlled by simply changing the incident angle. (3) The deposited film is self-aligned due to the shadowing effect.

During the experiment, glancing angle deposition of a TiO_2 layer with nanorod structures onto the sensor surface was performed in an e-beam deposition system (Denton Vacuum) with a base pressure of 2.0×10^{-6} Torr and a deposition rate of 0.8 nm/s. The sensor is tilted so that the incoming flux of evaporated material is at a glancing angle of $\theta = 10.0^{\circ}$ from the sensor surface.

4.3 Device Structure

As shown in Fig. 5.1, the DFBLB structure is comprised of a low refractive index UV-curable polymer grating (n = 1.38, period = 400 nm, depth = 160 nm) that is overcoated with a thin film of SU-8 (5.0 wt %; Microchem, n = 1.58, t = 400 nm) that is doped with a laser dye (Rhomamine 590, Exciton) as described in previous work [3]. The device preparation and fabrication are presented in previous chapters. The only difference in the device structure reported in this chapter is the TiO_2 nanorod coating. The TiO_2 nanorod layer is deposited on top of the gain layer by the GLAD technique as mentioned above. A scanning electron microscope image of a GLAD TiO_2 film deposited upon a DFBLB is shown in Fig. 4.1.

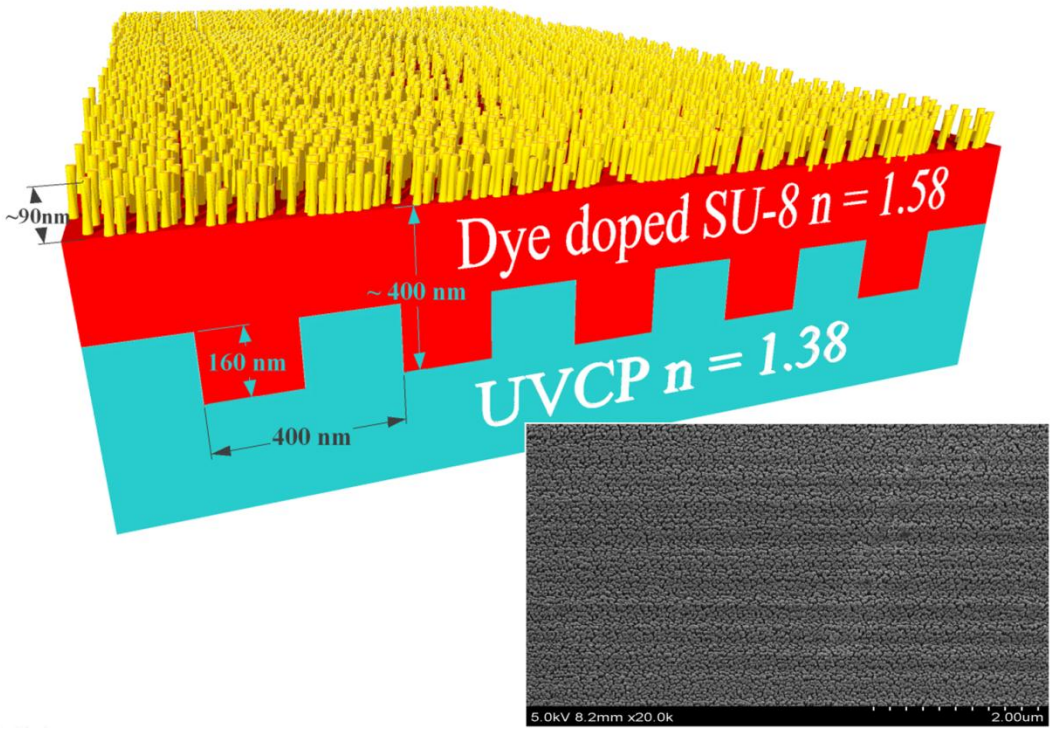

Fig. 4.1. Cross-sectional diagram of the DFBLB structure (not to scale). The period and depth of the grating structure are 400 nm and 160 nm, respectively. The sensor surfaces were coated with TiO2 nanorod films with thickness of 90 nm. An SEM image of the nanorod is also shown on the bottom.

A steady-state electric-field intensity cross-section profile at resonance was calculated using rigorous coupled-wave analysis (RCWA) for a device with a 30 nm TiO_2 nanorod coating, as shown in Fig. 4.2. The superstrate was water (n = 1.33) and an effective refractive index of n = 1.82 was used for the TiO_2 nanorod layer when immersed in water. The polarization of the calculated electrical field is parallel to the grating (TE polarization). The TE polarization was selected because the fundamental lasing mode is TE_0 mode. When the thickness of the TiO_2 nanorod layer is increased, the electromagnetic field distribution is altered, but only very slightly because the thickness of the TiO_2 nanorod layer (22 nm < t < 90 nm) is a small perturbation of the structure when compared to the dye doped SU-8 layer ($t \approx$ 400 nm) [4].

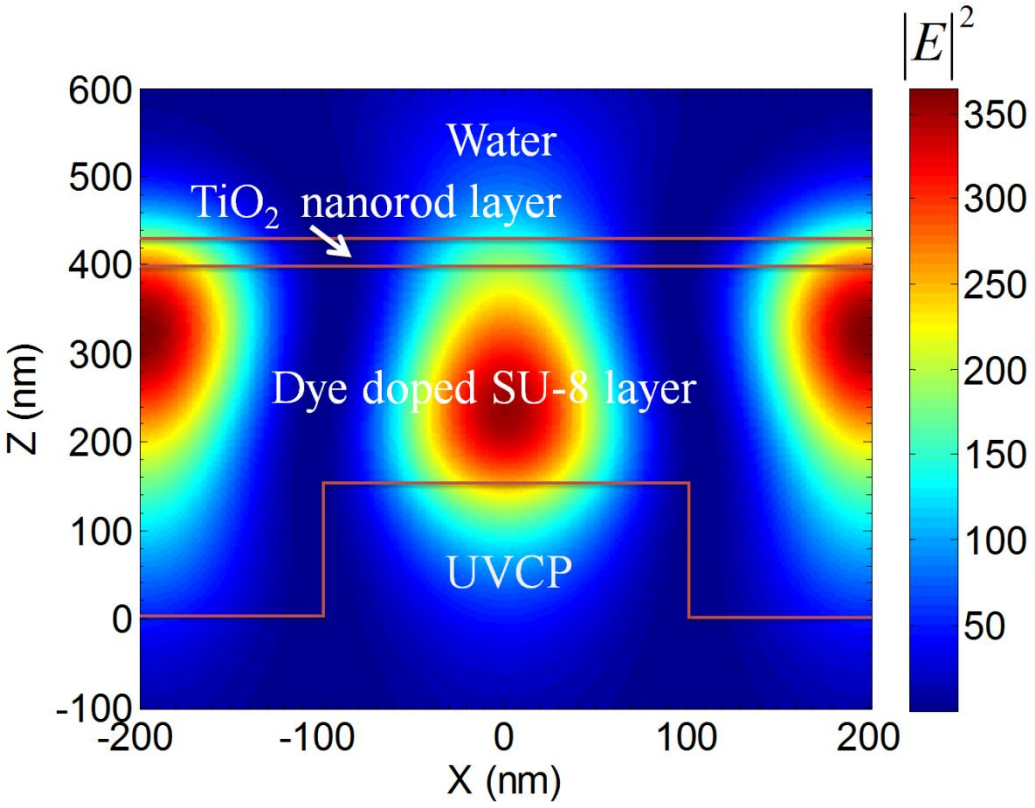

Fig. 4.2. Electric field intensity profile for a DFBLB with a 30 nm TiO_2 nanorod film.

4.4 Laser Emission Characterization

Figure 4.3 shows the laser emission spectrum of a DFBLB with a t = 90 nm nanorod coating and with sensor surface immersed in water. The observed lasing wavelength is at λ = 602.4513 nm and the full width half maximum (FWHM) is $\Delta\lambda \approx$ 0.0235 nm, corresponding to a Q-factor of 25,600. Here, both peak wavelength value (PWV) and FWHM of the emission spectrum are obtained by fitting the discrete measurements from the spectrometer with a Lorentzian model, enabling a peak fitting algorithm to obtain PWV shift resolution lower than the spectrometer resolution. The inset of Fig. 4.3 shows the dependence of the laser emission wavelength as a function of nanorod thickness. The

TiO_2 nanorod layer causes the PWV to shift to longer wavelength. Meanwhile, the linewidth of the emission spectrum remains as narrow as the DFB structure without a nanorod TiO_2 film coating. This indicates that the nanorods, with feature size far below the resonant wavelength of $\lambda \approx$ 600 nm, do not cause scattering or absorption that results in a measurable effect other than the addition of material with higher dielectric permittivity than water.

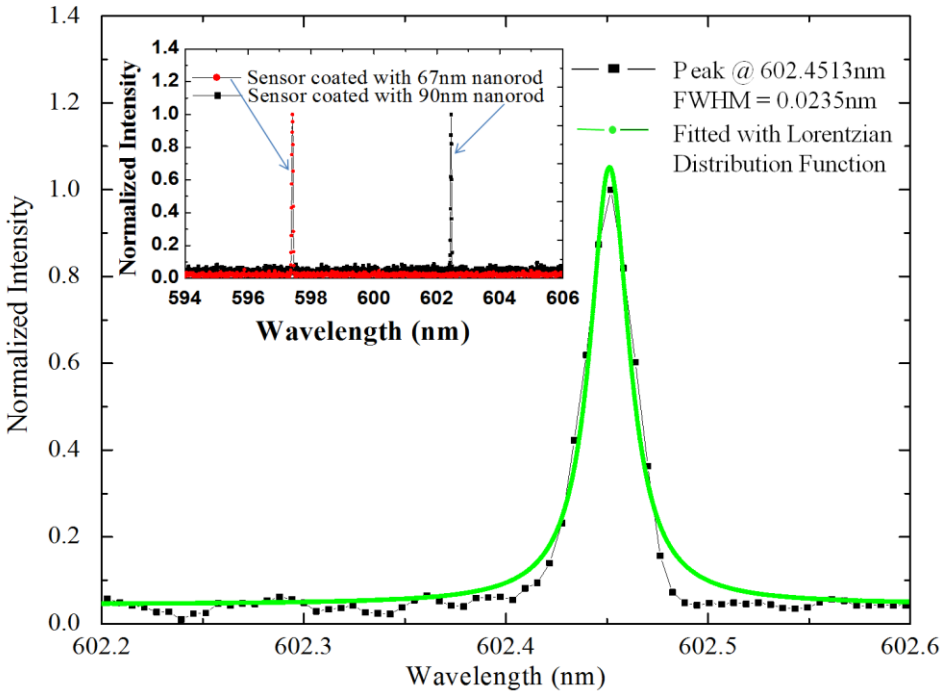

Fig. 4.3 DFB laser emission profile. The sensor was coated with 90 nm TiO_2 nanorod film and immersed in DI water. Inset shows the red-shift of PWV due to increased TiO_2 nanorod thickness.

4.5 Experimental Results

The DFBLB sheet is attached to a bottomless 96-well microplate with adhesive, so the DFBLB forms the entire bottom surface of each 6.7 mm diameter microplate well. The biosensor microplate is held in a fixture that is attached to an x-y motion stage, which

enables computer-programmed excitation of a precise location on the DFB surface. Within a single microplate well, the excitation laser separately probes 75 independent locations in an x-y rectangular grid with 400 μm spacing to compute the average PWV. Gathering the 75 measurements takes ~60 sec.

To demonstrate the sensitivity enhancement resulting from the TiO_2 nanorod layer, sensitivity to surface mass adsorption was characterized. Sensors with either a 30 nm solid TiO_2 film or nanorod TiO_2 films of 22 nm, 30 nm, 67 nm, 90 nm were prepared. All the sensors were coated with a single monolayer of protein using the following protocol. First, the sensors were exposed to a phosphate buffered saline (PBS) solution for 15 min, after which a baseline PWV measurement was taken from each biosensor microplate well, as described above. Next, the PBS solution was removed by pipette and the wells were refilled with 1 mg/ml solution of the protein polymer poly (Lys, Phe) (PPL) (Sigma–Aldrich). In previous research, PPL has been demonstrated to form a self-limiting single monolayer coating upon dielectric surfaces. PPL molecules have a molecular weight of 35,400 Da and a linear chain structure, and are therefore expected to penetrate the TiO_2 nanorod layer and to result in binding that is proportional to the available exposed surface area. Previous characterization of PPL films estimated that the film thickness is ~15 nm with a refractive index of ~1.45. The PPL solution was incubated with the sensor surfaces for 48 minutes, after which the PPL solution was removed and the sensor surface was rinsed with PBS solution three times to remove any PPL that was not firmly attached to the sensor surface. With PBS solution in the biosensor microplate wells, a second set of PWV measurements were gathered. Each

active biosensor microplate well that was exposed to PPL was accompanied by a reference well that was not exposed to PPL, in order to compensate for any possible common mode experimental artifacts (such as temperature variation) during the PPL incubation step. The PWV shift that is reported in Fig. 4.4 represents the wavelength shift difference between the active sensor and its reference, using $t = 0$ as a baseline. Overall, the reference sensor supplied very little correction, as no reference sensor had a shift of greater than 0.0283 nm during the 48 minutes incubation time. Our results show that thicker TiO_2 nanorod films result in the greatest PWV shift for adsorption of PPL, and the thickest nanorod layer (90 nm) results in a 6.6× enhancement in surface sensitivity. Importantly, as shown by the kinetic binding plots in Fig. 4.4, the 90 nm nanorod film does not appear to substantially limit the rate of monolayer adsorption, as the nanorod spacings are large enough to enable PPL molecules to enter without an evident diffusion limitation. Because the DFB lasing mode is predicted by RCWA models (not shown) to extend only ~100 nm into the nanorod layer, thicknesses of this magnitude are expected to optimize the PWV shift. Greater thickness of the nanorod layer will increase the available surface area, but at a cost of more difficult diffusion of molecules to the regions closest to the SU-8 upper surface, where interaction between adsorbed molecules and the resonant mode electric field is greatest.

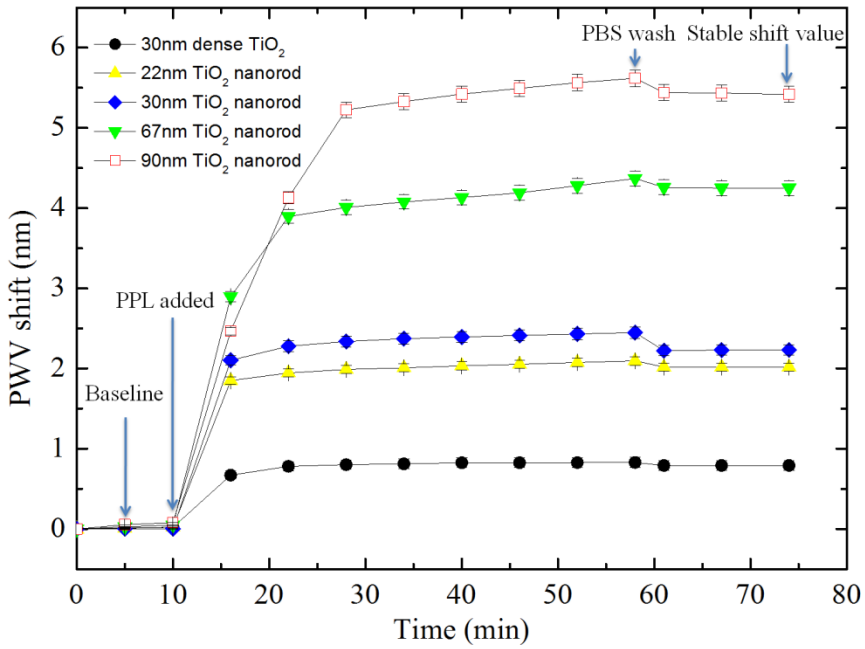

Fig. 4.4. Dynamic detection of adsorption of a polymer protein self-limiting monolayer for nonporous TiO_2 film coated and porous TiO_2 nanorod coated sensors.

4.6 Conclusion

In conclusion, the surface sensitivity of a DFBLB is enhanced by a device design that incorporates a porous TiO_2 nanorod layer on the sensor surface. Unlike previously reported DFBLBs with a solid smooth TiO_2 film that allows for two-dimensional volume overlap between the DFBLB resonant mode and the region where biomaterial adsorption occurs, such a porous structure enables a three-dimensional overlap. In order to demonstrate the surface sensitivity enhancement, a detection of a monolayer of protein polymer poly (Lys, Phe) was conducted. Results show that the sensitivity to surface mass adsorption increases as the nanorod film thickness increases and a 90 nm TiO_2 nanorod structure improves the detection sensitivity by a factor of 6.6 compared to an identical sensor with a nonporous TiO_2 surface.

4.7 References

[1] M. Lu, S. S. Choi, C. J. Wagner, J. G. Eden, and B. T. Cunningham, "Label free biosensor incorporating a replica-molded, vertically emitting distributed feedback laser," *Applied Physics Letters*, vol. 92, p. 261502, 2008.

[2] W. Zhang, N. Ganesh, I. D. Block, and B. T. Cunningham, "High sensitivity photonic crystal biosensor incorporating nanorod structures for enhanced surface area," *Sensors and Actuators B-Chemical*, vol. 131, pp. 279-284, 2008.

[3] M. Lu, S. S. Choi, U. Irfan, and B. T. Cunningham, "Plastic distributed feedback laser biosensor," *Applied Physics Letters*, vol. 93, 111113, 2008.

[4] I. D. Block, N. Ganesh, M. Lu, and B. T. Cunningham, "Sensitivity model for predicting photonic crystal biosensor performance," *IEEE Sensors Journal*, vol. 8, pp. 274-280, 2008.

CHAPTER 5

OUTLOOK

5.1 Small and Single Molecule Detection

Given the DFB laser biosensor's narrowband output, good sensitivity and the ability to be focused into a small volume, we can envision its potential applications in small molecule or even single molecule detection for adsorption of protein.

Single molecule experiments have been improving our understanding of the most fundamental biological processes such as protein folding kinetics [1], molecular transport [2], and aspects of DNA replication [3]. Recent technical advances in fluorescence detection have made the detection of isolated, light-emitting probe molecules a reality. Thus we are witnessing a continuously growing interest in the imaging and spectroscopy of single molecules, particularly within the fields of cell biology and drug discovery [4]. Although fluorescence-based detection is extremely sensitive, the molecule labeling process not only results in an extensive amount of work but also interferes with the function of the target biomolecule. Therefore, researchers have been developing label-free biosensors with single-molecule sensitivity, such as nano-scale field-effect transistors (FETs) made of semiconductor nanowires [5]. Here, we would like to investigate the potential for the DFB laser biosensors to perform label-free detection of small molecules or single molecules.

To calculate the detection capability, we first need to estimate the volume of liquid above the DFB biosensor surface that is probed by a single pulse from the excitation laser.

In the current DFB label-free biosensor system, the pumping light passes through a 10× beam expander and then is focused onto the DFB laser by a 20× Nikon objective (NA = 0.5) to minimize the excitation spot size. The theoretical pumping spot size can be calculated based on Equation (5.1)

$$W = \frac{4}{\pi} \cdot \lambda \cdot \frac{F}{D} \tag{5.1}$$

where W is the diameter of the pumping spot size, λ is the wavelength of the pumping light (532 nm), F is the focal length of the objective (0.55 mm) and D is the diameter of the pumping light beam (10 mm) incident on the objective. The one-dimensional DFB grating provides high optical confinement in the lateral direction. The effective penetration depth l_{eff} into one DFB grating end can be estimated by Equation (5.2)

$$l_{eff} = \frac{\lambda_o}{4 n_{eff} \Delta n} \tag{5.2}$$

where λ_o is the laser emission wavelength in vacuum, n_{eff} is the effective refractive index of the DFB cavity and $\Delta n = n_{\text{H}} - n_{\text{L}}$ is the modulation strength of the DFB grating.

In the transverse direction, we can approximate the penetration depth as the diameter of the pumping spot, W. Above the sensor surface, the evanescent optical field

decays exponentially and the penetration depth τ has been demonstrated to be ~200 nm in previous work [6].

Based on the analysis above, the liquid volume above the sensor surface that is probed by one single laser pulse can be calculated as

$$V = (2l_{eff} + W) \cdot W \cdot \tau \tag{5.3}$$

Theoretically, the sample volume V can be as small as ~8× 10^{-5} pL, when the pumping spot size is assumed to be near the diffraction limit which is ~$\lambda_o/2$ = 300 nm and a modulation strength of Δn = 0.2 is used.

In order to calculate the laser emission wavelength shift caused by a single molecule, the perturbation to the effective refractive index resulting from the binding of a single molecule should be calculated first. The effective index can be considered as a weighted average of the refractive indices of the materials in which the standing lasing wave is supported. The weighting is determined by the fractional electromagnetic intensity in each region.

$$n_{eff}^2 = \frac{\int_{-\infty}^{+\infty}\int_{-\frac{W}{2}}^{+\frac{W}{2}}\int_{-\frac{W}{2}-l_{eff}}^{\frac{W}{2}+l_{eff}} \varepsilon(x,y,z)\left|E(x,y,z)\right|^2 dxdydz}{\int_{-\infty}^{+\infty}\int_{-\frac{W}{2}}^{+\frac{W}{2}}\int_{-\frac{W}{2}-l_{eff}}^{\frac{W}{2}+l_{eff}} \left|E(x,y,z)\right|^2 dxdydz} \tag{5.4}$$

where $\varepsilon(x,y,z)$ and $E(x,y,z)$ are the three-dimensional spatial distributions of the dielectric permittivity and electric field. The grating is aligned in the x direction and the resonant mode penetrates into the surrounding medium in z direction.

The biosensor functions by measuring laser emission wavelength shifts due to effective index changes resulting from adsorbed biomaterial as given by the differential of the Bragg condition in Equation (1.2)

$$\Delta\lambda = \Delta n_{eff}\,\Lambda \tag{5.5}$$

Assuming the electric field only exists in the gain layer and evanescent range above sensor surface, then Equation (5.4) can be rewritten as

$$n_{eff}^2 = \frac{\int_{-d}^{0}\int_{-\frac{W}{2}}^{+\frac{W}{2}}\int_{-\frac{W}{2}-l_{eff}}^{\frac{W}{2}+l_{eff}} \varepsilon(x,y,z)\left|E(x,y,z)\right|^2 dxdydz}{\int_{-\infty}^{+\infty}\int_{-\frac{W}{2}}^{+\frac{W}{2}}\int_{-\frac{W}{2}-l_{eff}}^{\frac{W}{2}+l_{eff}} \left|E(x,y,z)\right|^2 dxdydz} + \frac{\int_{0}^{\tau}\int_{-\frac{W}{2}}^{+\frac{W}{2}}\int_{-\frac{W}{2}-l_{eff}}^{\frac{W}{2}+l_{eff}} \varepsilon(x,y,z)\left|E(x,y,z)\right|^2 dxdydz}{\int_{-\infty}^{+\infty}\int_{-\frac{W}{2}}^{+\frac{W}{2}}\int_{-\frac{W}{2}-l_{eff}}^{\frac{W}{2}+l_{eff}} \left|E(x,y,z)\right|^2 dxdydz} \tag{5.6}$$

where d is the depth of the gain layer and the sensor surface is at the plane of z = 0. The first part of Equation (5.6) is the contribution to the effective refractive index from the gain layer and the second part is that from the detection region above the sensor surface. For a single molecule binding, the assumption of no change in the electric field distribution should be valid. For analytical solution of the effective index change as a function of the change of $\varepsilon(x,y,z)$ resulting from molecules binding, the exact expression of the electric field distribution $E(x,y,z)$ is needed. Here, only some basic

calculation based on first order perturbation theory is provided to estimate the order of magnitude of the laser emission wavelength shift caused by single molecule attaching. In addition, some reasonable assumptions supported by the RCWA simulation results are also applied to simplify the problem.

After the binding of a single molecule, the effective refractive index becomes n'_{eff}, which can still be divided into two parts: one part is the integral of the dielectric permittivity times the electric field intensity inside the gain layer; the second part is the integral in the detection region, as shown in Equation (5.7)

$$n'_{eff} = \left(\frac{\int_{-d}^{0}\int_{-\frac{W}{2}}^{+\frac{W}{2}}\int_{-\frac{W}{2}-l_{eff}}^{\frac{W}{2}+l_{eff}} \varepsilon(x,y,z)\left|E(x,y,z)\right|^2 dxdydz}{\int_{-\infty}^{+\infty}\int_{-\frac{W}{2}}^{+\frac{W}{2}}\int_{-\frac{W}{2}-l_{eff}}^{\frac{W}{2}+l_{eff}} \left|E(x,y,z)\right|^2 dxdydz} + \frac{\int_{0}^{\tau}\int_{-\frac{W}{2}}^{+\frac{W}{2}}\int_{-\frac{W}{2}-l_{eff}}^{\frac{W}{2}+l_{eff}} \varepsilon'(x,y,z)\left|E(x,y,z)\right|^2 dxdydz}{\int_{-\infty}^{+\infty}\int_{-\frac{W}{2}}^{+\frac{W}{2}}\int_{-\frac{W}{2}-l_{eff}}^{\frac{W}{2}+l_{eff}} \left|E(x,y,z)\right|^2 dxdydz}\right)^{1/2} \quad (5.7)$$

where $\varepsilon'(x,y,z)$ is the new permittivity distribution function above the sensor surface. The function $\varepsilon'(x,y,z)$ can be expressed as the summation of the initial $\varepsilon(x,y,z)$ and the perturbation term $\Delta\varepsilon(x,y,z)$ introduced by the molecule:

$$\varepsilon'(x,y,z) = \varepsilon(x,y,z) + \Delta\varepsilon(x,y,z) \quad (5.8)$$

where $\Delta\varepsilon(x,y,z)$ is the difference of dielectric permittivity between the biomolecule such as a protein and the surrounding medium:

$$\Delta\varepsilon(x,y,z) = (n_{protein})^2 - (n_{medium})^2 \quad (5.9)$$

If a protein with a refractive index of $n_{protein}$= 1.45 immersed in DI water (n_{medium}= 1.33) is investigated, then $\Delta\varepsilon(x,y,z)$ = 0.33 within the volume occupied by this protein. An analytical expression for $\Delta\varepsilon(x,y,z)$ is

$$\Delta\varepsilon(x,y,z)=\int_{-\infty}^{+\infty}\int_{-\infty}^{+\infty}\int_{-\infty}^{+\infty} f(x,y,z)\delta(x-x')\delta(y-y')\delta(z-z')\Delta\varepsilon dx'dy'dz' \tag{5.10}$$

where $f(x,y,z)$ is the spatial distribution function of the protein and $\Delta\varepsilon = 0.33$ is the constant of the permittivity difference.

$$f(x,y,z)=\begin{cases}1 & \text{occupied}\\ 0 & \text{not occupied}\end{cases} \tag{5.11}$$

Substituting Equations (5.8), (5.9), (5.10) and (5.11) into Equation (5.7), n'_{eff} can be rewritten as

$$n'_{eff}=\left(\frac{\int_{-d}^{0}\int_{-\frac{W}{2}}^{+\frac{W}{2}}\int_{-\frac{W}{2}-l_{eff}}^{\frac{W}{2}+l_{eff}}\varepsilon(x,y,z)\left|E(x,y,z)\right|^2 dxdydz}{\int_{-\infty}^{+\infty}\int_{-\frac{W}{2}}^{+\frac{W}{2}}\int_{-\frac{W}{2}-l_{eff}}^{\frac{W}{2}+l_{eff}}\left|E(x,y,z)\right|^2 dxdydz}+\frac{\int_{0}^{\tau}\int_{-\frac{W}{2}}^{+\frac{W}{2}}\int_{-\frac{W}{2}-l_{eff}}^{\frac{W}{2}+l_{eff}}\varepsilon(x,y,z)\left|E(x,y,z)\right|^2 dxdydz}{\int_{-\infty}^{+\infty}\int_{-\frac{W}{2}}^{+\frac{W}{2}}\int_{-\frac{W}{2}-l_{eff}}^{\frac{W}{2}+l_{eff}}\left|E(x,y,z)\right|^2 dxdydz}\right.$$

$$\left.+\frac{\int_{0}^{\tau}\int_{-\frac{W}{2}}^{+\frac{W}{2}}\int_{-\frac{W}{2}-l_{eff}}^{\frac{W}{2}+l_{eff}}\Delta\varepsilon(x,y,z)\left|E(x,y,z)\right|^2 dxdydz}{\int_{-\infty}^{+\infty}\int_{-\frac{W}{2}}^{+\frac{W}{2}}\int_{-\frac{W}{2}-l_{eff}}^{\frac{W}{2}+l_{eff}}\left|E(x,y,z)\right|^2 dxdydz}\right)^{1/2}$$

$$= \left(\frac{\int_{-d}^{0}\int_{-\frac{W}{2}}^{+\frac{W}{2}}\int_{-\frac{W}{2}-l_{eff}}^{\frac{W}{2}+l_{eff}} \varepsilon(x,y,z)\left|E(x,y,z)\right|^2 dxdydz}{\int_{-\infty}^{+\infty}\int_{-\frac{W}{2}}^{+\frac{W}{2}}\int_{-\frac{W}{2}-l_{eff}}^{\frac{W}{2}+l_{eff}} \left|E(x,y,z)\right|^2 dxdydz} + \frac{\int_{0}^{\tau}\int_{-\frac{W}{2}}^{+\frac{W}{2}}\int_{-\frac{W}{2}-l_{eff}}^{\frac{W}{2}+l_{eff}} \varepsilon(x,y,z)\left|E(x,y,z)\right|^2 dxdydz}{\int_{-\infty}^{+\infty}\int_{-\frac{W}{2}}^{+\frac{W}{2}}\int_{-\frac{W}{2}-l_{eff}}^{\frac{W}{2}+l_{eff}} \left|E(x,y,z)\right|^2 dxdydz}\right.$$

$$\left. + \frac{\int_{0}^{a}\int_{-a/2}^{+a/2}\int_{-a/2}^{+a/2} \Delta\varepsilon(x,y,z)\left|E(x,y,z)\right|^2 dxdydz}{\int_{-\infty}^{+\infty}\int_{-\frac{W}{2}}^{+\frac{W}{2}}\int_{-\frac{W}{2}-l_{eff}}^{\frac{W}{2}+l_{eff}} \left|E(x,y,z)\right|^2 dxdydz}\right)^{1/2}$$

$$= \left(n_{eff} + \frac{\int_{0}^{a}\int_{-a/2}^{+a/2}\int_{-a/2}^{+a/2} \Delta\varepsilon(x,y,z)\left|E(x,y,z)\right|^2 dxdydz}{\int_{-\infty}^{+\infty}\int_{-\frac{W}{2}}^{+\frac{W}{2}}\int_{-\frac{W}{2}-l_{eff}}^{\frac{W}{2}+l_{eff}} \left|E(x,y,z)\right|^2 dxdydz}\right)^{1/2} \tag{5.12}$$

where the single molecule is assumed to occupy an a^3 cubic. According to the first order perturbation theory, Equation (5.12) can be further simplified as

$$n'_{eff} = n_{eff} + \frac{1}{2}\frac{\int_{0}^{a}\int_{-a/2}^{+a/2}\int_{-a/2}^{+a/2} \Delta\varepsilon(x,y,z)\left|E(x,y,z)\right|^2 dxdydz}{\int_{-\infty}^{+\infty}\int_{-\frac{W}{2}}^{+\frac{W}{2}}\int_{-\frac{W}{2}-l_{eff}}^{\frac{W}{2}+l_{eff}} \left|E(x,y,z)\right|^2 dxdydz} \tag{5.13}$$

Therefore, the introduced effective refractive difference due to the single molecule binding is

$$\Delta n_{eff} = n'_{eff} - n_{eff} = n_{eff} + \frac{1}{2}\frac{\int_{0}^{a}\int_{-a/2}^{+a/2}\int_{-a/2}^{+a/2}\Delta\varepsilon(x,y,z)\left|E(x,y,z)\right|^2 dxdydz}{\int_{-\infty}^{+\infty}\int_{-\frac{W}{2}}^{+\frac{W}{2}}\int_{-\frac{W}{2}-l_{eff}}^{\frac{W}{2}+l_{eff}}\left|E(x,y,z)\right|^2 dxdydz} - n_{eff}$$

$$= \frac{1}{2}\frac{\int_{0}^{a}\int_{-a/2}^{+a/2}\int_{-a/2}^{+a/2}\Delta\varepsilon(x,y,z)\left|E(x,y,z)\right|^2 dxdydz}{\int_{-\infty}^{+\infty}\int_{-\frac{W}{2}}^{+\frac{W}{2}}\int_{-\frac{W}{2}-l_{eff}}^{\frac{W}{2}+l_{eff}}\left|E(x,y,z)\right|^2 dxdydz} \tag{5.14}$$

Assuming (1) a = 15 nm, (2) the gain layer depth d = 400 nm, (3) the electric field is quasi-uniformly distributed inside the gain layer with an intensity twice that on top of the sensor surface (supported by the RCWA simulation) and (4) the electric field exponentially decays from the sensor surface, then an $\Delta n_{eff} \approx 6 \times 10^{-4}$ can be roughly estimated based on Equation (5.14). Furthermore, a laser emission wavelength shift ~10 pm can be predicted based on Equation (5.5). Previous research has demonstrated a wavelength shift detection limit as low as 9.8 pm [7]. Therefore, detection resolution sufficient for observing attachment of a single protein molecule is theoretically possible!

The analysis above is based on the physical modeling of the problem. Additionally, this problem can also be tackled using an experiment based method, as the following analysis shows.

Previous research has successfully detected a ~1 nm laser emission wavelength shift for a self-limited, single monolayer protein having a refractive index, thickness and

mass density of 1.45, 15 nm, and 2.5 ng mm^{-2} [7, 8]. Within the linear response region of the biosensor, the laser emission wavelength shift is linearly proportional to the surface mass density of the attached protein, with a surface sensitivity s_{surf} defined as

$$s_{surf} = \frac{\Delta\lambda}{\rho_{surf}} = \frac{1 \text{ nm}}{2.5 \text{ ng/mm}^2} = 0.40 \text{ nm} \cdot \text{mm}^2/\text{ng} \tag{5.15}$$

where ρ_{surf} is the surface mass density. Then a wavelength shift detection limit of 9.8 pm will correspond to a surface mass density detection limit as low as

$$\rho_{surf} = \frac{\Delta\lambda}{s_{surf}} = \frac{9.8 \text{ pm}}{0.4 \text{ nm} \cdot \text{mm}^2/\text{ng}} = 24.5 \text{ pg/mm}^2 \tag{5.16}$$

As calculated above, the smallest surface are probed by one laser pulse is

$$S = (2l_{eff} + W) \cdot W \tag{5.17}$$

Then a surface mass detection limit of ~9.55 $\times 10^{-6}$ pg. can be estimated. If the protein investigated has a molecule weight of 450,000 Da, then it means ~12.62 protein molecules can be detected.

5.2 DFB Label-Free Biosensor for High-Resolution Imaging

Besides the applications in small molecules detection, another advantage of the DFB laser biosensor is its ability to perform high-resolution spatial imaging. Since the DFB pump laser can be focused on a small spot, it possesses the ability to monitor the

morphology of the sensor with applications in high-resolution cell imaging and gene/protein array imaging in a fashion functionally similar to fluorescent confocal laser scanner instruments.

As analyzed above, the spatial resolution in the lateral direction of the DFB laser could be approximated by $2l_{eff} + 2W$, where $2l_{eff}$ is the effective penetration depth into the ends of DFB gratings and $2W$ is the diameter of the pumping spot. In this situation, the spatial resolution is theoretically limited by the penetration depth $2l_{eff}$, which is in the scale of ~1 μm.

To perform high-resolution spatial imaging, we have established a new experimental platform with an automated two-dimensional translation stage with 0.3 μm step increments and a corresponding control program written in C# language. Figure 5.1 is an image of the detection setup. A user interface panel of the developed computer control program is shown in Fig. 5.2. This program is able to synchronize the Nd:YAG pulsed laser pumping and Horiba Yvon iHR550 spectrometer detection, analyze measured spectra, and calculate the emission wavelength shift. After receiving data from the spectrometer, our program first normalizes the spectrum and generates a fit using the standard Lorentzian function to find peak emission value with a resolution better than the resolution of the iHR550 spectrometer. The Lorentzian function is given by $y = y_0 + cw/[4(\lambda - \lambda_0)^2 + w^2]$, where λ_0 represents the calculated lasing emission peak value. Since the surface absorption of protein, DNA sequences, or attaching of cells will register a local laser emission wavelength shift, we can characterize the surface

morphology of the device by measuring the laser emission spectrum as a function of the spatial location, so as to get a label-free detection image.

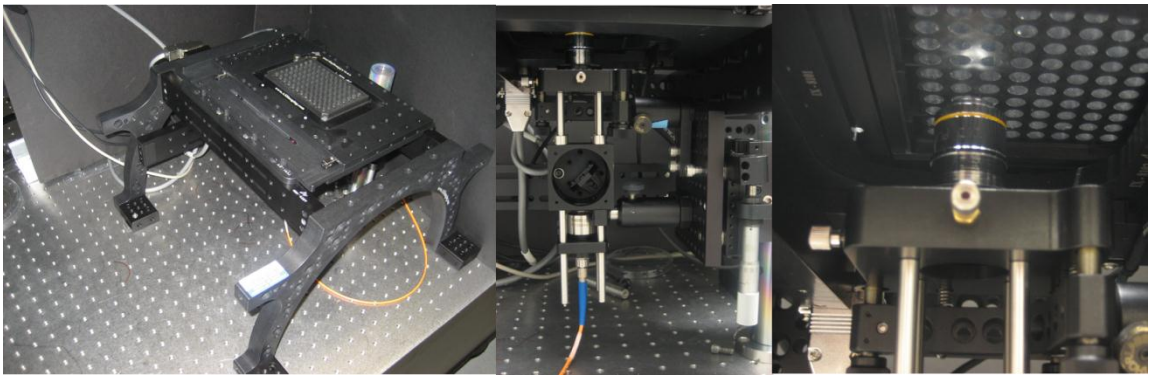

Fig. 5.1 Top view, side view and bottom view of the detection setup.

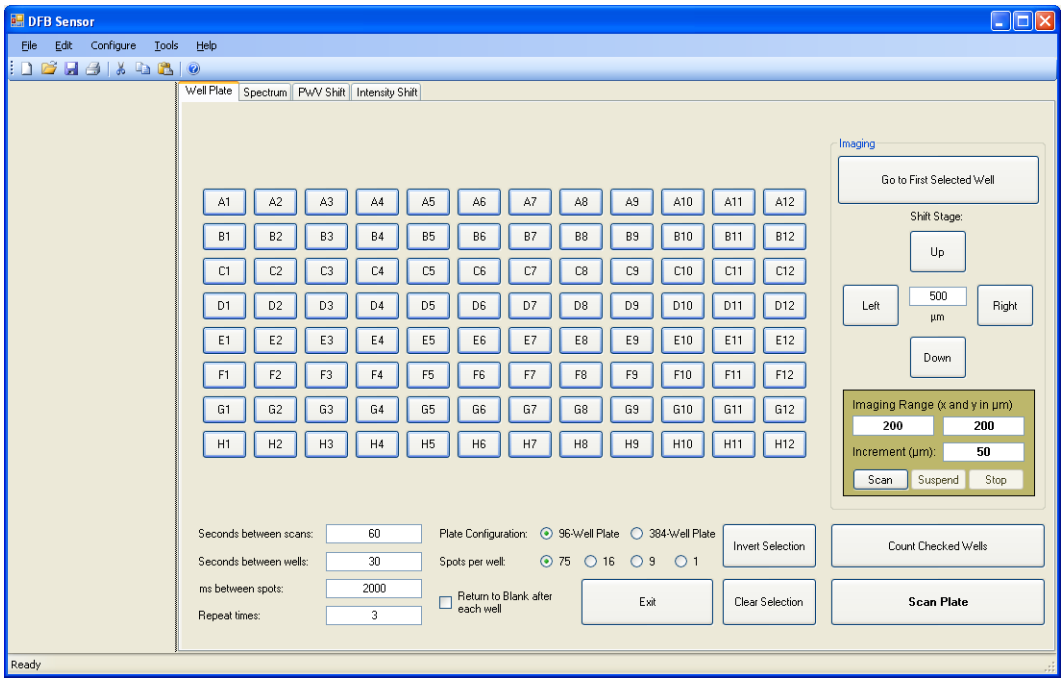

Fig. 5.2 User interface of the control software.

There are two inherent challenges associated with this imaging scheme that must be carefully addressed in order to optimize performance. One is the careful control of the size of the pumping spot. For high-resolution imaging, we need to minimize this spot

size. As Equation (5.1) indicated, the spot size is inversely proportional to the beam diameter of the input pumping light to the objective and linearly related to the focal length of the objective. Therefore, in order to get a minimized pumping spot, we need to expand the beam diameter as large as possible and choose an objective with short focal length or working distance. In our setup, a 10× beam expander is utilized to expand the pumping light and an objective with 5 mm working distance is chosen. However, from Gaussian optics we know that the smaller the focused beam size, the higher the divergence, as indicated by Equations (5.18) and (5.19),

$$\theta = \frac{\lambda}{\pi W} \tag{5.18}$$

$$b = \frac{2\pi W^2}{\lambda} \tag{5.19}$$

where θ is the divergence of the beam and b is the depth of focus of the beam. Therefore, a focus distance self-adjustment scheme needs to be introduced to account for the focusing distance change due to the nonuniformity of the device surface caused by device fabrication or any other reasons. A possible scheme could be to use an inverted microscope to dynamically monitor the pumping spot size and adjust the position of the focusing objective or the sensor chip accordingly.

Another challenge posed by this imaging scheme is the data acquisition speed. Since this is a sequential data acquisition scheme, the acquisition speed is much slower than other parallel data acquisition schemes. The data acquisition speed is limited by a few parameters including the speed of the translation stage, the integration time of the

CCD inside the spectrometer and the pumping rate. In our situation, the ultimate limiting factor is the pumping rate, which is up to only 10 Hz as limited by the Q-switch scheme used to produce the nanosecond pumping pulses. In other words, we can only take 10 measurements each second. Given a 1 μm step increment and a 1 mm × 1 mm scanning area, the image acquisition time is estimated to be ~10^5 seconds, which is more than 27 hours! Therefore, in the future, either a parallel pumping and detection scheme or a pumping source with higher pumping rate is needed to perform the biological detection that requires short data acquisition time, such as taking a label-free image of live cells. However, if a much smaller field of view is needed, such an imaging scheme is able to give a high-resolution label-free image with quantitative information of the dynamic attaching of biomolecules.

5.3 References

[1] J. Wang, Q. Lu, and H. P. Lu, "Single-molecule dynamics reveals cooperative binding-folding in protein recognition," *PLoS Computational Biology*, vol. 2, p. 78, 2006.

[2] J. K. Jaiswal and S. M. Simon, "Imaging single events at the cell membrane," *Nature Chemical Biology*, vol. 3, pp. 92-98, 2007.

[3] M. J. Lang, P. M. Fordyce, A. M. Engh, K. C. Neuman, and S. M. Block, "Simultaneous, coincident optical trapping and single-molecule fluorescence," *Nature Method*, vol. 1, pp. 133-139, 2004.

[4] W. E. Moerner, "New directions in single-molecule imaging and analysis," *Proceedings of the National Academy of Sciences*, vol. 104, pp. 12596-12602, 2007.

[5] F. Patolsky, G. Zheng, O. Hayden, M. Lakadamyali, X. Zhuang, and C. M. Lieber, "Electrical detection of single viruses," *Proceedings of the National Academy of Sciences of the United States of America*, vol. 101, pp. 14017-14022, 2004.

[6] M. Lu, S. S. Choi, U. Irfan, and B. T. Cunningham, "Plastic distributed feedback laser biosensor," *Applied Physics Letters*, vol. 93, p. 111113, 2008.

[7] M. Lu, S. Choi, C. J. Wagner, J. G. Eden, and B. T. Cunningham, "Label free biosensor incorporating a replica-molded, vertically emitting distributed feedback laser," *Applied Physics Letters*, vol. 92, p. 261502, 2008.

[8] C. Ge, M. Lu, W. Zhang, and B. T. Cunningham, "Distributed feedback laser biosensor incorporating a titanium dioxide nanorod surface," *Applied Physics Letters*, vol. 96, pp. 163702, 2010.